FH University of Applied Sciences TECHNIKUM WIEN

MASTER THESIS

Thesis submitted in fulfillment of the requirements for the degree of Master of Science in Engineering at the University of Applied Sciences Technikum Wien - Degree Program Data Science

Multi-sensor rail track detection in automatic train operations

By: Attila Kovacs

Student Number: 2110854031

Supervisors: Lukas Rohatsch
Daniele Capriotti

Wien, February 29, 2024

Declaration

“As author and creator of this work to hand, I confirm with my signature knowledge of the relevant copyright regulations governed by higher education acts (see Urheberrechtsgesetz /Austrian copyright law as amended as well as the Statute on Studies Act Provisions / Examination Regulations of the UAS Technikum Wien as amended).

I hereby declare that I completed the present work independently and that any ideas, whether written by others or by myself, have been fully sourced and referenced. I am aware of any consequences I may face on the part of the degree program director if there should be evidence of missing autonomy and independence or evidence of any intent to fraudulently achieve a pass mark for this work (see Statute on Studies Act Provisions / Examination Regulations of the UAS Technikum Wien as amended).

I further declare that up to this date I have not published the work to hand nor have I presented it to another examination board in the same or similar form. I affirm that the version submitted matches the version in the upload tool.“

Wien, February 29, 2024 Signature

Kurzfassung

Die Erhöhung des Automatisierungsgrades im Bahnbetrieb ist ein Schlüsselfaktor für die Erreichung eines effizienteren und wettbewerbsfähigeren Eisenbahnsystems. Automatische Zugbetriebssysteme (ATO) nutzen fortschrittliche Technologien, um die Eisenbahnumgebung wahrzunehmen und zu interpretieren und um autonome Betriebsabläufe mit minimalem menschlichem Eingriff zu ermöglichen. Die präzise Identifizierung und Lokalisierung von Eisenbahngleisen sind grundlegend für eine sichere Zugnavigation. Daher besteht Bedarf an robusten automatisierten Methoden zur Gleiserkennung.

Diese Masterarbeit befasst sich mit der Aufgabe der Mehrsensorschienenverfolgung im Rahmen von ATO durch die Nutzung von Deep-Learning-Techniken, insbesondere der semantischen Segmentierung. Durch die Erforschung eines Mehrsensordatensatzes, der Bilder von hoch-/niedrigauflösenden RGB-Kameras und Infrarotkameras mit unterschiedlichen Orientierungen umfasst, zielt diese Forschung darauf ab die Genauigkeit und Robustheit der Gleiserkennung unter verschiedenen Bedingungen zu verbessern. Die Studie vergleicht die Leistung der Deep-Learning-basierten Segmentierung mit traditionellen nicht KI-basierten Methoden, führt umfassende Bewertungen verschiedener Sensorinputs durch und erforscht die Integration in realen Anwendungen. Die Ergebnisse liefern wertvolle Erkenntnisse auf dem Gebiet der Eisenbahnautomatisierung und bieten Implikationen zur Verbesserung der Sicherheit und Effizienz des automatischen Zugbetriebs.

Schlagworte: Deep Learning, Computer Vision, Segmentation, Automatic Train Operations

Abstract

Increasing the level of automation in train operations is an enabler in achieving a more efficient and competitive railway system. Automatic train operations (ATO) systems use advanced technologies to perceive and interpret the railway environment in order to facilitate autonomous operations with minimal human intervention. Precise identification and localization of railway tracks are fundamental for safe train navigation. Hence there is a need for robust automated track detection methods.

This master's thesis addresses the task of multi-sensor rail track detection within the ATO framework by utilizing deep learning techniques, particularly semantic segmentation. By exploring a multi-sensor dataset comprising images from high/low-resolution RGB cameras and infrared cameras with varying orientations, this research aims to improve the accuracy and robustness of track detection in diverse conditions. The study compares the performance of deep learning-based segmentation with traditional non-AI-based methods, conducts comprehensive evaluations on different sensor inputs, and explores real-world application integration. The findings contribute valuable insights to the field of railway automation, offering implications for enhancing the safety and efficiency of automatic train operations.

Keywords: Deep Learning, Computer Vision, Rail Track Segmentation, YOLO, Automatic Train Operations

Contents

1 Introduction

According to the International Energy Agency (IEA), the global demand for passenger and freight transportation will more than double by 2050 compared to 2019 (International Energy Agency, 2019). However, a greater demand entails higher energy consumption as well as increased CO2 emissions and atmospheric pollutants. Given the fact that railway is one of the most efficient and reliable modes of transportation there seems to be consensus between politicians and researchers that a greater reliance of rail has the potential to counterbalance the negative impacts of transportation (Islam et al., 2016; Pagand et al., 2020). The IEA lists minimizing costs per passenger-kilometer or ton-kilometer moved as one of three pillars that are essential to increase the market share of rail transportation[1].

Automatic Train Operations (ATO) which refers to a system that automates different aspects of train operations is expected be one of the key drivers of a more efficient and competitive railway system (ALSTOM Transport SA, 2021; Europe's Rail Joint Undertaking, 2019). ATO is estimated to reduce energy consumption by up to 45%, increase the level of punctuality, increase operational flexibility, and allow for a 50% better utilization of the infrastructure when combined with other technologies.

ATO relies on advanced technologies that are used to perceive and interpret the railway environment in order to allow autonomous operations with minimal or no human intervention (Deutsche Bahn AG, 2022). One aspect of ATO is the precise identification and localization of railway tracks. The ability to detect and isolate tracks based on video images is essential for ensuring the safe navigation of trains through the railway network or in shunting yards. Accurate track detection ensures that the train can make informed decisions, such as adjusting speed, navigating turns, and responding to potential obstacles.

Traditional methods of track detection often rely on rule-based algorithms and image processing techniques, but these approaches may face challenges in diverse environmental conditions such as bad weather, complex background, lighting variations

[1] The other pillars are maximizing revenues from rail systems, and ensuring that all forms of transport (especially road transportation) pay not only for the use of the infrastructure they need, but also for the adverse impacts they generate.

(e.g., day and night), and dirty cameras. This master's thesis addresses the task of multi-sensor rail track detection in the context of ATO. We explore deep learning techniques, particularly convolutional neural networks (CNNs), that have demonstrated great success in computer vision tasks, including image segmentation. The application of deep learning to track detection is expected to outperform conventional non-AI-based techniques and thereby improving the accuracy and robustness of the system. Our analysis is based on a multi-sensors dataset, including images of normal RGB cameras, high-resolution cameras, and infrared cameras, with different orientations, respectively. This multi-sensor approach allows to compare the the effectiveness of different cameras and informs the deployment of those in order to improve the robustness of track detection in diverse conditions.

In the context of rail track detection, researchers have explored various areas. Yet, applying deep learning techniques to detect rail tracks is a relatively raw field. In particular, there is no research that is focusing on comparing different input images such as RGB and infrared cameras and images that are oriented to the left, center, and right of the locomotive. The contribution of this thesis to the literature is three-fold: First, we select and train a deep learning model capable of accurately detecting and segmenting railway tracks using data from RGB cameras, high-resolution cameras, and infrared cameras. In contrast to approaches that have been specifically tailored to the task, we apply a general framework that is easier to use by practitioners without elaborate software engineering skills. The results of the deep learning model are compared to a non-AI based method specialized in identifying lines in images. Second, we conduct a comprehensive performance evaluation to assess the accuracy and computational efficiency of the proposed track detection system on images generated by different cameras. Third, we explore the integration of the developed model into real-world applications by applying to identify tracks in video streams.

By achieving these objectives, this research provides valuable insights and advancements to the field of railway automation, with implications for improving the safety and efficiency of automatic train operations.

2 Literature review

Traditionally, rail track detection has been performed by first extracting features of an image (e.g., gradient-based thresholds) and then detecting rails. These approaches achieve good results in certain conditions. However, deep-learning based approaches are often more robust in real-world environments (Giben et al., 2015; Li and Peng, 2022; Wang et al., 2019). Deep learning techniques, particularly CNNs, have emerged as powerful tools for image segmentation tasks, demonstrating success in various computer vision applications. Recent surveys on image segmentation and object detection using deep-learning techniques is provided by Cheng et al. (2023) and Zaidi et al. (2022), respectively.

The following sections examine related research in track detection, considering both deep learning-based segmentation and traditional non-AI segmentation methods.

2.1 Traditional rail track detection

While deep learning has shown remarkable success in track detection, non-AI segmentation techniques continue to play a role in this field as they allow the integration of domain-specific knowledge and rules into the algorithm and require less data for training. These methods are often referred to as line segment detectors and involve traditional computer vision techniques such as thresholding, edge/contour detection, template matching, and region growing (Almazàn et al., 2017; Grompone von Gioi et al., 2010, 2012; Mittal et al., 2022; Sahoo et al., 1988).

Kaleli and Akgul (2009) present a dynamic programming algorithm to extract the rail tracks in front of the train. The idea is to first identify the vanishing point which refers to the imaginary intersection of the tracks as the distance between the tracks decreases from the bottom of the image to the top. This step is based on computing the gradient and applying Hough transform to detect the straight lines that indicate the tracks. Next, dynamic programming is used to extract the space between the two tracks. Qi et al. (2013) apply a method based on histogram of oriented gradients (HOG) to identify tracks and switches. First, HOG features are computed; railway tracks are then identified by a region-growing algorithm. The proposed method is able to predict the patch the train will travel by detecting the setting of the switches. Nassu and Ukai (2011) introduce an approach that performs rail extraction by matching edge features to candidate templates.

While the previously mentioned approaches focus on images by on-board cameras, Purica et al. (2017) examines the detection of tracks in aerial images taken by drones. The solution approach is based on Hough transform.

(Arastounia, 2015) and (Yang and Fang, 2014) develop methods to recognize railroad infrastructure from 3D LIDAR data. In (Arastounia, 2015), railway components such as rail tracks, contact cables, catenary cables, masts, and cantilevers are classified based on local neighborhood structure, shape of objects, and topological relationships among objects. (Yang and Fang, 2014) focus on the detection of tracks. The authors utilize the geometry and reflection intensity of the tracks to extract features and identify tracks.

2.2 Deep-learning based rail track detection

Deep-learning based techniques such as semantic segmentation incorporate convolutional neural networks (CNNs) and other deep architectures to automatically learn features from raw image data. Semantic segmentation aims to assign a label to each pixel in the image, distinguishing between the pixels that belong to the rail tracks and those that represent the background and is therefore particularly well suited for rail track detection.

Giben et al. (2015) and Le Saux et al. (2018) were among the first authors who evaluated the performance of deep learning-based segmentation against traditional segmentation techniques in rail track detection. In Giben et al. (2015), the authors propose a CNN for localizing and inspecting the condition of railway component based on gray-scale images. The authors report that the CNN model is better suited to capture complex patters compared to approaches that rely on traditional texture features (e.g., discrete Fourier transforms of local binary pattern histograms). Le Saux et al. (2018) detect rail tracks in aerial images by devising a CNN based approach and different traditional approaches such as thresholding.

Wang et al. (2019) propose the RailNet – a deep-learning based rail track segmentation algorithm that combines the ResNet50 backbone with a fully convolutional network. In order to train the model, the authors compile a non-public dataset consisting of 3000 images from forward-facing on-board cameras. Experiments show that RailNet is able to outperform general purpose models for segmentation. In Li and Peng (2022), the authors compile a real-world railway dataset based on which a rail detection method referred to as Rail-Net is devised. Rail-Net outperforms traditional methods by around 51% and other deep-learning methods by around 6% based on accuracy when applied

on the newly developed dataset.

A machine-learning based approach is proposed by (Teng et al., 2016) where features are extracted from super-pixels (i.e., a group of adjacent pixels with similar characteristics) and classified by applying a previously trained support vector machine.

2.3 Lane detection

Lane detection for road vehicles is similar to rail track detection for locomotives in the sense that both tasks aim to identify and segment elongated shapes in complex environments that vary in lighting conditions, shadows, and occlusions. The field of lane detection has a rich body of literature which is among others attributed to the existence of well-established benchmark datasets such as TuSimple (2017) and CULane (Pan et al., 2018).

Early work on lane detection is based on traditional approaches such as Hough transform and clustering (Duda and Hart, 1972; Ma and Xie, 2010). Recently, the focus of researchers has shifted to deep-learning based approaches (Meyer et al., 2021; Wang et al., 2022; Zheng et al., 2022). Tang et al. (2021) and Yang (2023) provide comprehensive surveys on lane detection approaches. In (Yang, 2023), the authors propose a combined approach in which the advantages of traditional and deep-learning based methods are mixed.

3 Datasets

Labeled images are an essential prerequisite for training deep-learning algorithms to detect objects accurately. With the growing popularity of deep-learning, we have observed the creation of new datasets specifically designed for railway applications.

The rail semantics dataset 2019 (RailSem19) is the first publicly available dataset for detecting objects (including rail tracks) in the railway domain (Zendel et al., 2019). The French railway signaling dataset (FRSign) is a dataset focusing only on traffic lights (Zendel et al., 2019), whereas the Railway Pedestrian Dataset (RAWPED) is focusing on pedestrian detection methods (Toprak et al., 2020). The dataset proposed by Wang et al. (2019) – railroad segmentation dataset – has been compiled for the development

railroad segmentation algorithms but it is not available to the public. The Rail-DB dataset is available upon request (Li and Peng, 2022). The dataset comprises 7.432 annotated images, featuring different scenarios (e.g., weather conditions).

This thesis is based on the first freely available multi-sensor dataset “Open Sensor Data for Rail 2023” (OSDaR23) for the development of fully automated driving in the railway sector (Deutsche Bahn AG, 2023; Tagiew et al., 2023). Unlike the previously mentioned dataset that involve a limited number of sensors and perspectives, the system on the locomotive used to create the OSDaR23 dataset includes multiple infrared cameras, RGB cameras with different resolution, lidar, radar, positioning, and acceleration sensors.

Preliminary experiments indicated that our model fails to generalize when trained only on the OSDaR23 dataset due to reasons that will be described in the next section. Therefore, we also train our model on images from the RailSem19 dataset. In the following, we give a detailed description of the two datasets used in this thesis.

3.1 OSDaR23 dataset

3.1.1 Overview

The OSDaR23 contains 21 video sequences captured around Hamburg, Germany between 09.09.2021 and 15.09.2021 (a map of the exact locations is given in Figure 1). The sensor setup is very comprehensive including six RGB cameras, three IR cameras, six lidar sensors, a 2D radar sensor, and position and acceleration sensors. In this thesis, we focus on images by RGB high resolution, RGB low resolution, and infrared sensors with three orientation (left, right, and center), respectively. One example per sensor is given in Figure 2. A detailed description of the sensors can be found in Appendix A.1.

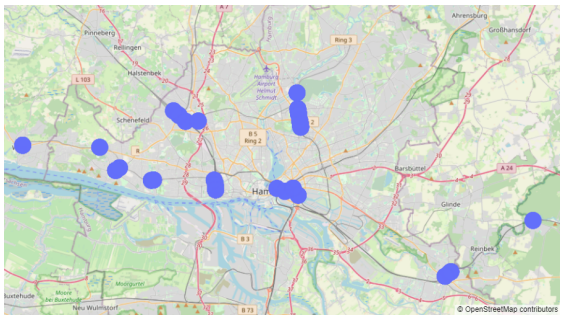

Figure 1: Locations where images were captured around Hamburg, Germany.

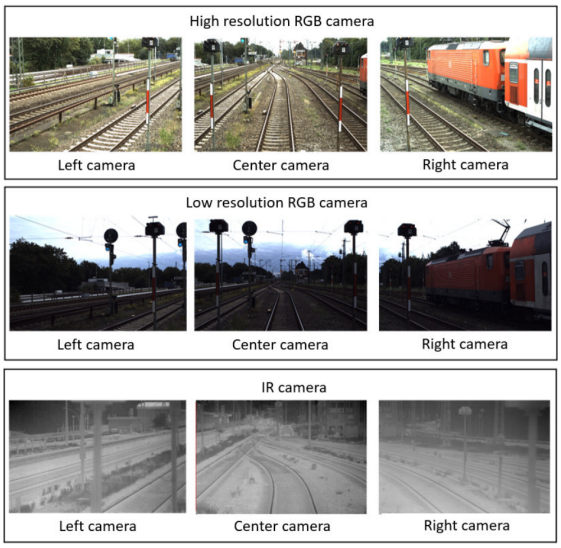

Figure 2: Example images of high resolution RGB, low resolution RGB, and infrared sensors (Tagiew et al., 2023).

The final number of images and labels after filtering the dataset, i.e., removing images that do not contain annotated tracks, is 7.421 and 27.386, respectively. The distribution of images and labels per sensor is displayed in Figure 3. The size of the images is given in Table 1. Figure 4 illustrates the number of track labels per image. Most images contain track pairs. However, there are also images with odd number of tracks. The largest group are images containing one pair of tracks. Generally, the number of available images decreases as the rail network is getting more complicated.

Sensor	Widht [px]	Height [px]	Aspect ration
RGB low resolution	4112	2504	1.64
RGB high resolution	2464	1600	1.54
Infrared	640	480	1.33

Table 1: Size of images per sensor.

All images were taken between 8AM and 17PM, so we cannot expect to test the effect of different sensors in the night. In particular, the RGB cameras fail to capture clear and detailed images in low-light conditions. Infrared cameras on the other hand, detect infrared radiation emitted by objects based on their temperature rather than visible light

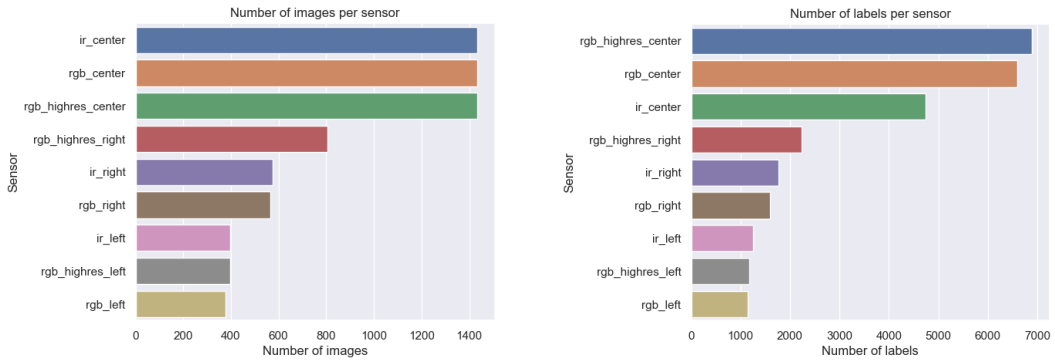

(a) Number of images per sensor

(b) Number of labels per sensor

Figure 3: Number of images and labels per sensor, respectively.

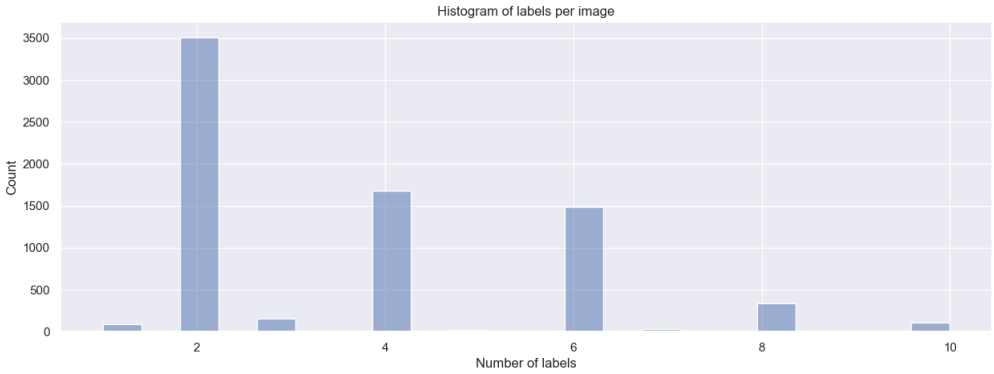

Figure 4: Track labels per image. Most images depict track pairs. However, there are also images with odd number of tracks.

and are, therefore, used in low-light conditions or complete darkness[1]. The thermal radiation is converted into electrical signals which are then processed to a visual image that is visible to the human eye (Clark et al., 2002). Warmer areas are displayed as brighter, while cooler areas appear as darker shades of gray.

Emissivity, a material property that indicates how efficiently an object emits infrared radiation, plays a significant role in thermal imaging. Emissivity is measured on a scale from 0 to 1, where 0 indicates a perfect reflection of the radiation (no emission such as a mirror), and 1 indicates perfect emissivity (total emission in an object referred to as blackbody). Detecting rail tracks in infrared images is based on the principle that polished metallic surfaces such as tracks have a low emissivity, whereas organic materials that appear often in the background have a high emissivity.

[1]All objects with a temperature greater than absolute zero emit infrared energy.

3.1.2 Brightness of the images

In deep learning, the quality of the images can have a large impact on the efficiency. Image segmentation tasks, where the goal is to identify and classify each pixel in an image, are particularly sensitive to variations in pixel brightness and intensity. In this section, we analyze the brightness of the images for each type of sensor. Brightness is defined as the average pixel intensity $\frac{1}{N}\sum_{i=1}^{N} I_i$; N is the number of pixels in the image, and I_i is the intensity of pixel i. In Figure 5 shows a series of box plots with brightness values per sensor.

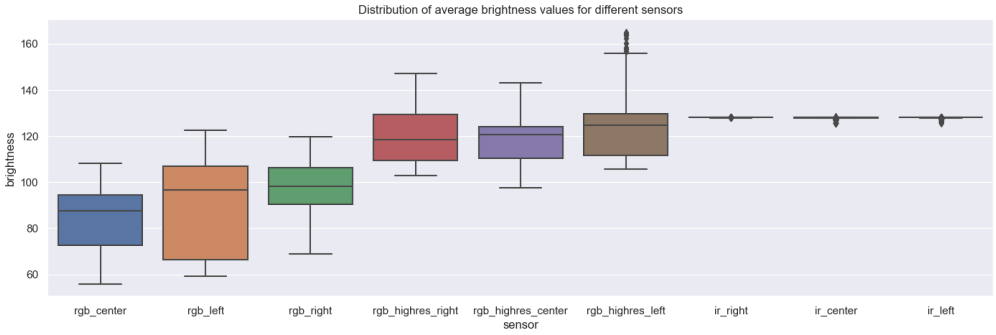

Figure 5: Brightness of images by sensor.

Among the three types of sensors, low resolution RGB cameras produce the darkest images (a black image has a value of 0, a white image has a value of 255). High resolution images are brighter on average, which can be explained by different exposure settings such as shutter speed and ISO sensitivity. Both low and high-resolution cameras feature pixels of equal size $(3.45\mu m)$, so the amount of light per pixel is the same. Infrared cameras produce images with almost constant brightness as the non-visible infrared image is mapped on a visible spectrum.

Figure 6 show one example of a bright and a dark image, respectively.

3.1.3 Entropy of the images

Shannon entropy is a measure from information theory that reflects the uncertainty or randomness associated with a set of data (Shannon, 1948). In the context of images, Shannon entropy can be used to quantify the complexity in the pixel values of an image. A high entropy value indicates higher complexity or randomness in the pixel values, while a low entropy value suggests more homogeneity. Rahane and Subramanian (2020) report a positive correlation between the entropy of the training data and the performance

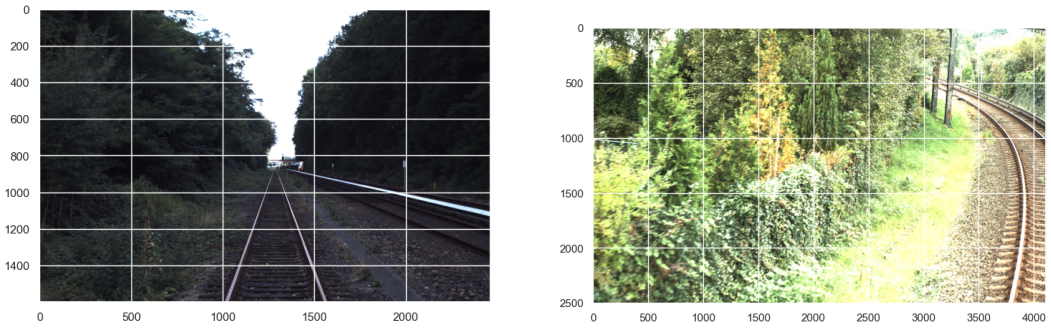

(a) Image with low brightness value.

(b) Image with high brightness value

Figure 6: Examples of very bright and very dark image, respectively.

of semantic segmentation tasks, highlighting that more complex images are harder to learn by deep-learning networks. The Shannon entropy for a grayscale image is given by $H(X) = -\sum_{i=1}^{n} P(x_i) \cdot \log_2(P(x_i))$, where $P(x_i)$ is the probability of occurrence of pixel x_i (i.e., the number of pixels with intensity x_i divided by the total number of pixels). A box-plot with the entropy distribution is given in Figure 8 for each sensor. The maximum entropy value is $8 = \log_2(256)$ as we convert the images to grayscale with 256 different intensity levels.

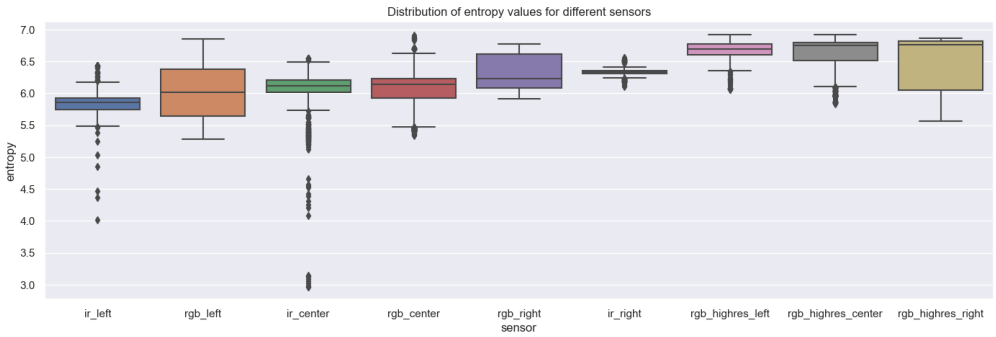

Figure 7: Entropy of images by sensor.

Overall, the images have a high entropy – the median values range from 5.9 to 6.8. High resolution images have the highest entropy. Infrared images do not seem to have lower entropy on average. However, certain images seem to have a very low randomness; and as it turns out also very low level of information when looking at Figure 8a. Figure 8 highlight the visual difference between a very low and a very high entropy image.

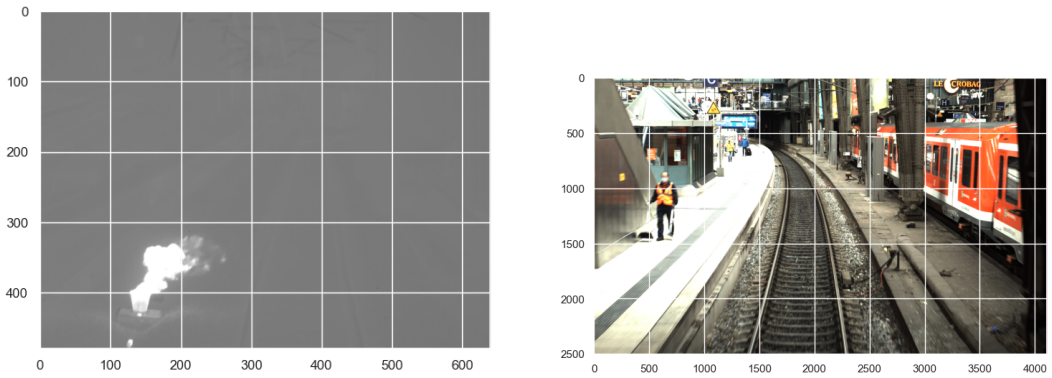

(a) Image with low entropy value.

(b) Image with high entropy value

Figure 8: Examples of image with minimal and maximal entropy, respectively.

3.1.4 Occlusion

Certain track labels are hidden or occluded by other objects. One example is given in Figure 8b where the train on the right covers the tracks. In this section, we analyze the occlusion of the labels and examine those occlusions visually.

Figure 9 shows the number of labels with a given occlusion level. Most of the labels, 20.069, are not occluded at all or have only a slight occlusion. However, 320 labels in 196 images are marked with an occlusion level of 100%. Figure 10 shows two examples where the track labels are fully covered.

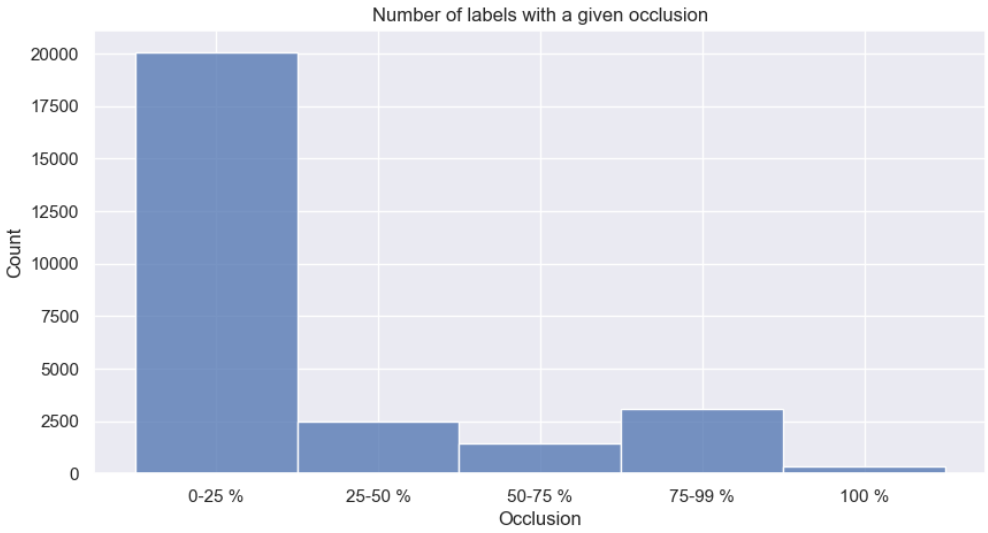

Figure 9: Histogram showing the occlusion level for track labels.

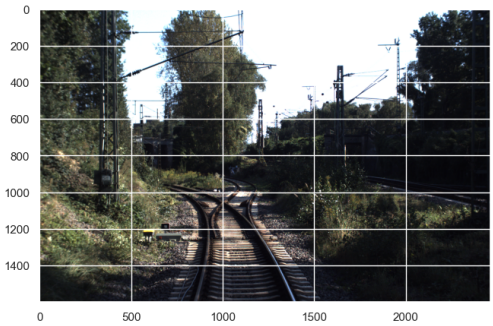

(a) Track on the right is hard to recognize due to poor lighting condition.

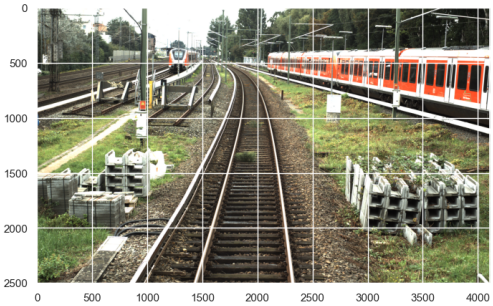

(b) Track is covered by train on the right.

Figure 10: Examples of track labels with 100% occlusion.

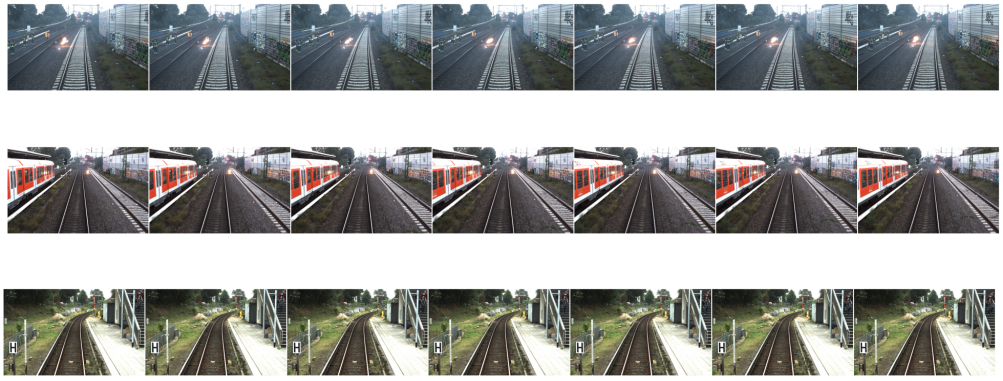

Figure 11: Three examples with seven video frames (i.e., images), respectively.

We keep all images in the dataset as the CNN might recognize that there has to be a track below a train and because most images with covered labels have visible labels as well.

3.1.5 Images and video frames

The rail tracking systems aim to analyze video streams by treating each video frame as an independent image. Consequently, the images in the OSDaR23 dataset represent individual frames extracted from video sequences. Figure 11 shows three examples of video sequences with seven frames each. It is clear to see that there is only minor variation in the images.

Two major issues when training a model on a dataset that consists of similar images is a lack of generalization (i.e., inability to generalize well on diverse and unseen images)

and reduced robustness (i.e., vulnerability to variations in lighting conditions and backgrounds). In order to mitigate the issues, we add images from the RailSem19 dataset to the training data.

3.2 RailSem19 dataset

The RailSem19 dataset (Zendel et al., 2019) is not the primary focus on of this thesis. However, the previous analysis reveals that among the 7,421 images within the OSDaR23 dataset, a significant number show high similarity. This similarity is due to the fact that the images are frames from a video sequence and the presence of three cameras for each orientation, respectively. The RailSem19 dataset is added to the training set in order to increase the performance of the segmentation approach. In the following, we will examine the RailSem19 dataset in more detail.

The dataset consists of 8500 rail images, taken in different countries, and weather and lighting conditions. The number of rail annotations is 58.483. All images have a size of 1920x1080 pixels. Figure 12 shows a histogram of images with the respective number of track labels. Most images contain 4 track labels (i.e., two pairs of tracks) but the dataset also contains complicated networks with 26 pairs of tracks. An example of a simple and an example of a complicated infrastructure is given in Figure 13.

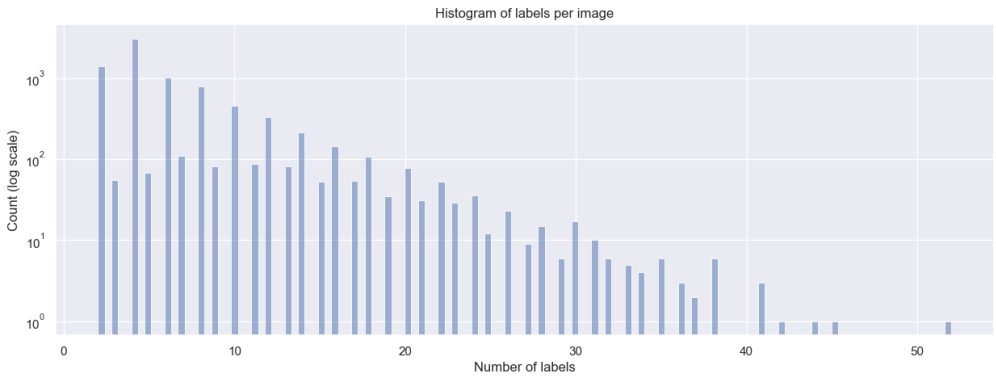

Figure 12: Track labels per image on a logarithmic scale. The images range from simple railroads with a single pair of tracks to complicated networks with 26 pairs of tracks.

Figure 14a and Figure 14b show the distribution of the brightness values and the entropy values as defined in Section 3.1, respectively. The RailSem19 images are mostly brighter than the OSDaR23; the distribution of the values ranges from almost black images to almost white images (see Figure 15a and Figure 15a). The entropy of

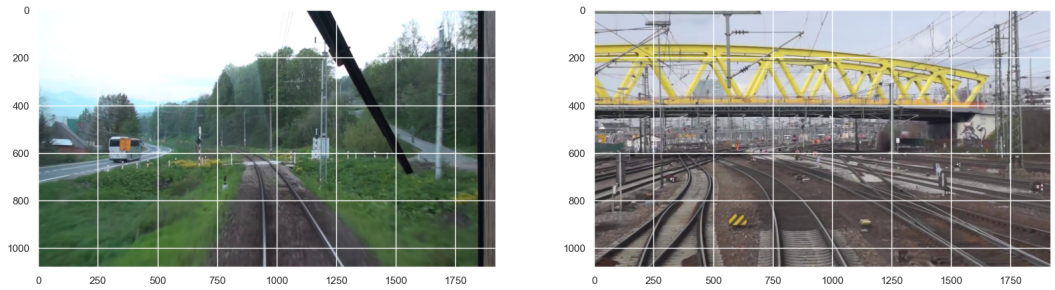

(a) Simple rail infrastructure.

(b) Complicated rail infrastructure.

Figure 13: Examples of simple and complicated rail infrastructure.

the RailSem19 images is similar to the images in the OSDaR23 dataset. The outliers at the lower end of the entropy spectrum are associated with infrared images in the OSDaR23 dataset. Howerver, in RailSem19 low entropy images are often images that were generated in tunnels or at night. Figure **??** and Figure **??**) are images with a low entropy levels close to zero whereas Figure **??**) has the highest entropy level in the data set with a score of 6.97.

3.3 Data splitting

Splitting a dataset into training, validation, and test sets is a standard practice in machine learning to evaluate and improve the performance of a model. Separating data into distinct sets and using them at different stages of development, prevents unintended data leakage where information from the test or validation set influences the training process.

The validation set assesses performance during training, refines hyperparameters, and guards against overfitting. Adjustments made based on validation set evaluations ensure the model generalizes effectively to new, unseen data.

The training set is used to train the model – the model learns patterns and relationships within the training data. The validation set is used to evaluate the performance during the training process, fine-tune the hyperparameters of the model, and to prevent overfitting (i.e., a situation when a model performs well on the training data but fails to generalize to new data). We can make adjustments to the algorithm and optimize the performance on the validation set without compromising the model's ability to generalize to new data. The test set is reserved for the final evaluation of the model. The test set allows for an unbiased assessment of the model's performance on data it has never seen before

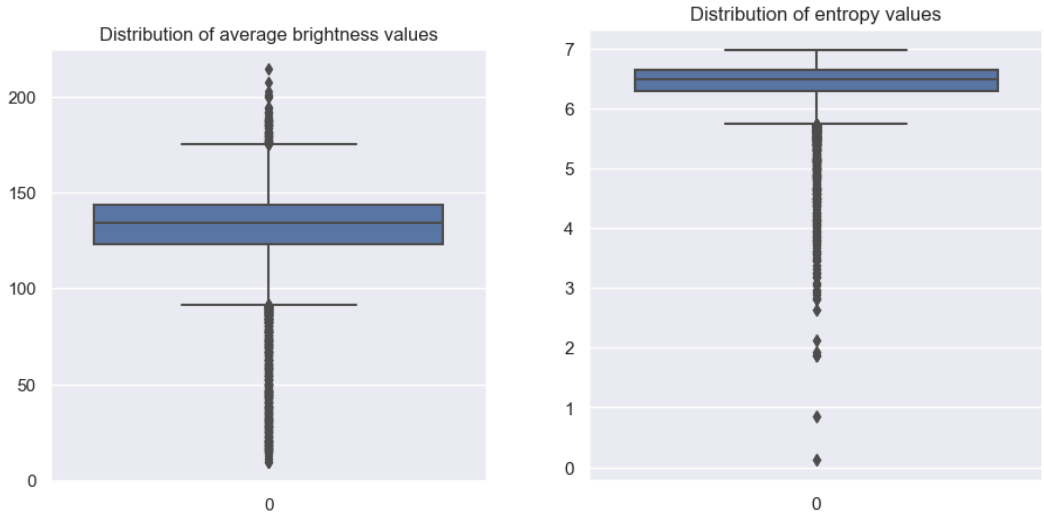

(a) Boxplot of brightness values.

(b) Boxplot of entropy values.

Figure 14: Brightness and entropy of RailSem19 images.

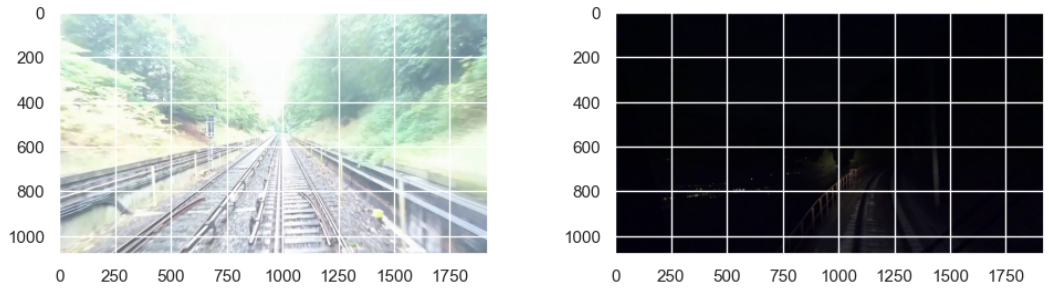

(a) Bright image.

(b) Dark image.

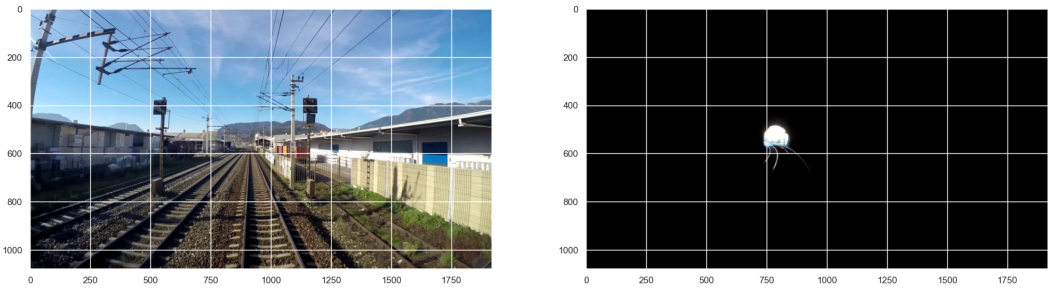

(c) High entropy.

(d) Low entropy.

Figure 15: Extreme examples with regard to brightness and entropy.

and provides, therefore, an estimate of how well the model is likely to perform on new, real-world data.

Our approach is to perform a random split with a share of 70%/15%/15% for train, validation, and test set respectively. Splitting the RailSem19 set is straightforward; we randomly assign images to each set resulting in 5.950, 1.275, and 1.275 images per set, respectively. However, the OSDaR23 comprises many images with high similar (e.g., frames from a video that was take when the locomotive was standing still), so we perform a random split not on individual images but on videos sequences. The approach results in 5.506 images for training, 987 images for validation, and 928 images for testing. The assignment of video sequences to the respective set and the split on sensor level is given in Appendix A.2

4 Solution approach and experiments

Given an image captured by an on-board camera on the locomotive, our objective is to precisely delineate the visible rail tracks. The output is a polyline describing each track.

Meyer et al. (2021) introduce YOLinO, a versatile and efficient algorithm inspired by single-shot object detection. It is designed to detect polylines in the context of lane detection, as discussed in Section 2.3. While the proposed approach is suitable for rail track detection, adapting the existing codebase from lane detection to rail track detection exceeds the scope of this thesis. Furthermore, our goal is to employ an off-the-shelf solution framework that can be readily utilized by a broader audience.

Within computer vision, semantic segmentation is a well-studied domain focusing on classifying each pixel in an image into predefined categories (Mo et al., 2022). Conceptually, it can be seen as an extension of object detection, a technique that recognizes and precisely locates objects within an image using bounding boxes. The pixel-level precision in object classification enables the understanding of the image context and is therefore often used in applications like autonomous driving and robotics.

Our approach to the rail detection problem is based on two steps. First, we perform a semantic segmentation where each pixel is classified as either rail track or background. In a second step, the result of the segmentation task is used to define one polyline for each track. Segmentation is performed by the YOLOv8 algorithm (Jocher et al., 2023). YOLOv8, short for "You Only Look Once, version 8," is the latest version in

the YOLO series of real-time object detectors, offering state-of-the-art performance in terms of accuracy and speed (Ultralytics Inc., 2023). YOLOv8 builds upon the YOLO architecture, introduced in Redmon et al. (2016) – a paper that has received more than 43.000 citations. Since the introduction of the original YOLO in 2016, the framework has been tested extensively with remarkable results (Diwan et al., 2023; Feng et al., 2022; Jiang et al., 2022). The efficiency of the YOLO implementations by Jocher et al. (2023) for segmentation tasks is examined in Yue et al. (2023) and Straker et al. (2023).

In order to compare the YOLO approach, we devise a track detection algorithm based on the fast line detector (FLD) by OpenCV (2024b). In the following, we describe the YOLO and the FLD approach, and give details of the infrastructure for running the experiments.

4.1 Infrastructure

Experiments are run on the High Performance Lab Cluster (HPL) of the UAS Technikum Wien. The HPL comprises 19 PCs connected through a 10-GBit-Network. The PCs have the following setup, respectively: AMD Ryzen 9 3900X 12-Core Processor, NVIDIA GeForce RTX 2080 Ti GPU, 32 GB RAM, and 80 GB Hard Disk.

All nodes are running Linux Ubuntu 20. CUDA libraries are installed for GPU management; the programming language is Python 3.8.10.

4.2 Transforming labels

In semantic segmentation, labels are often represented as closed polygons. Each polygon corresponds to a specific semantic class, and the pixels enclosed within the polygon are assigned the label of that class. However, the track labels in both OSDaR23 and RailSem19 dataset are given as polylines. Therefore, we transform the labels as follows. First, we adjust the thickness of the polyline such that is covers the tracks. Second, we generate the mask – a binary image where each pixel is assigned a value indicating the category it belongs to (i.e., track or background). Finally, the boundaries of the track label are exacted by using the $drawContours$ and $approxPolyDP$ functions in the OpenCV library, and the vectors defining the polygons are written to disk. Figure 24 illustrates the transformation process.

The presented approach generates polygons based on the segmentation mask. In order to test the effect of the labeling strategy, we also generate labels for each rail track

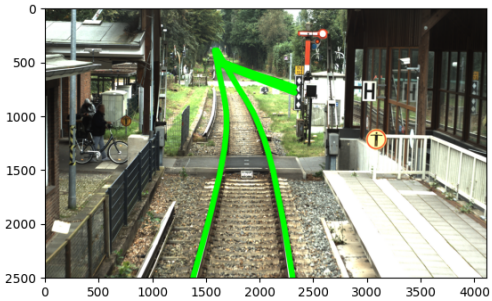

(a) Estimate thickness of such that the lines cover the tracks.

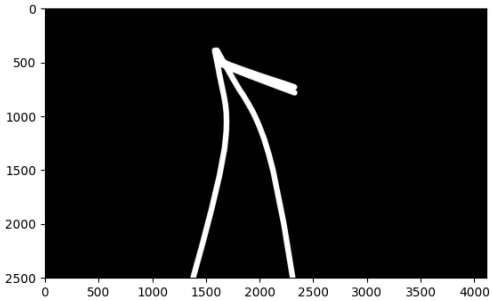

(b) Create mask (i.e., binary mapping of track labels and background).

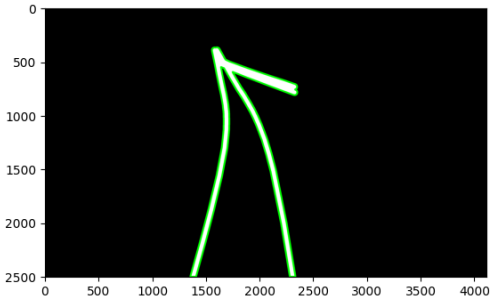

(c) Extract contour of track label (see green boundary in mask).

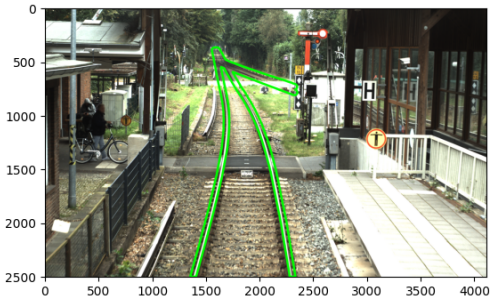

(d) Polygon is enclosing the region of interest.

Figure 16: Process of transforming the labels from polyline to polygon.

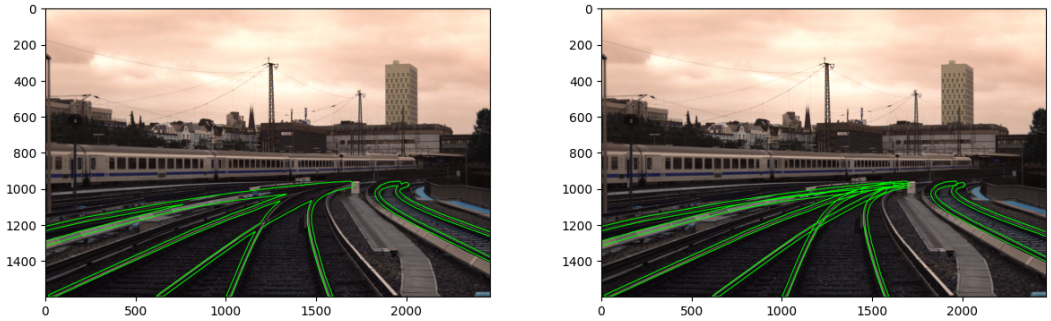

(a) All tracks are labeled by two closed polygons. (b) Each track is labeled by a separate polygon.

Figure 17: Two different approaches for labeling tracks.

label separately. Figure 17 illustrates the two labeling approaches. The unified polygon base on the mask is shown on the left; on the right, each track is labeled separately.

4.3 Performance evaluation

There is a number of performance metrics that are used in semantic segmentation to evaluate the effectiveness of the models (Taha and Hanbury, 2015). The choice of metrics typically depends on the specific requirements of the application and the nature of the dataset. In this section, we will introduce and examine different metrics.

Pixel Accuracy provides a simple measure of the overall accuracy by considering correctly predicted pixels.

$$\text{Pixel Accuracy} = \frac{\text{Number of Correctly Predicted Pixels}}{\text{Total Number of Pixels}}$$

Precision measures the accuracy of positive predictions among all positive predictions. The metric is important when minimizing false positives is critical such as in medical diagnostics.

$$\text{Precision} = \frac{\text{TP}}{\text{TP} + \text{FP}}$$

True Positives (TP) are the instances where the model correctly predicts the positive class (i.e., it correctly identifies the track). False Positives (FP) are the instances where the model incorrectly predicts the positive class (i.e., it incorrectly identifies a track when

it is actually absent).

Recall measures the ability to capture all positive instances. Recall is optimized when it is crucial to identify all instances of a particular class, even at the cost of some false positives.

$$\text{Recall} = \frac{\text{TP}}{\text{TP} + \text{FN}}$$

False Negatives are the instances where the model incorrectly predicts the negative class (i.e., it incorrectly identifies background even when the there is a track).

Dice score or F1 score, balances precision and recall which is particularly useful when dealing with unbalanced datasets, i.e., when one class has a much larger or smaller number of pixels compared to the other class (in our case background vs. tracks). Some authors use the Dice score while others use the F1 score with the respective formulas. However, it can be shown that one reduces to the other. Dice is the most used metric in segmentation when the dataset is unbalanced (e.g., medical imaging).

$$\text{Dice Score} = \frac{2 \times \text{TP}}{2 \times \text{TP} + \text{FP} + \text{FN}}$$

$$\begin{aligned} \text{F1 Score} &= \frac{2 \times \text{Precision} \times \text{Recall}}{\text{Precision} + \text{Recall}} \\ &= \frac{2 \cdot \frac{\text{TP}}{\text{TP}+\text{FP}} \cdot \frac{\text{TP}}{\text{TP}+\text{FN}}}{\frac{\text{TP}}{\text{TP}+\text{FP}} + \frac{\text{TP}}{\text{TP}+\text{FN}}} \\ &= \frac{2 \cdot \text{TP}}{2 \cdot \text{TP} + \text{FP} + \text{FN}} \end{aligned}$$

Intersection over Union (IoU) or Jaccard index, measures the overlap between predicted and ground truth regions. The metric is commonly used to evaluate the spatial accuracy of segmentation masks. Apart from the boundary values {0,1}, the IoU score is consistently smaller than the Dice score.

$$\text{IoU} = \frac{\text{TP}}{\text{TP} + \text{FP} + \text{FN}}$$

In Figure 18 we illustrate the concept of performance metric based on an example. Figure 18a shows the ground truth label, i.e., the correct pixels of the image being analyzed. Figure 18b, shows five potential predictions, where Image 5 is simply a black image with no positive classifications. The metrics for the five predictions are given in

Figure 18c. The example shows that Pixel accuracy is not appropriate in unbalanced dataset – even Image 5 which has no prediction at all has an accuracy score of almost 95%. Image 2 yields a high Precision score of 0.706 as the FN values are not accounted for. Recall seems to be a strong predictor of performance in this example. However, an all white image (i..e, all pixels classified as track) would yield a perfect Recall. Dice and IoU are best suited to distinguish between good and bad predictions. Both values have a wide range and the scores are in line with the estimation based on visual inspection.

Based on the literature and the example, we choose the Dice score to analyze the performance of different models.

4.4 Non-AI based segmentation

To assess the performance of the YOLO approach, we establish a baseline using a traditional line detection method. Specifically, we employ the fast line detection algorithm based on Hough transform, as implemented by OpenCV (2024b). In a post-processing step, we incorporate domain specific knowledge to improve the results. In this section, we describe the baselining approach in detail.

4.4.1 Fast line detection

The fast line detection algorithm as proposed by **?** operates as follows: First, edges in the image are detected using a Canny edge detector. The system then extracts line segments by connecting edge pixels with straight lines and extending them until they satisfy co-linearity conditions (i.e., whether or not the newly added pixels align well with the existing segment in terms of forming a straight line). Points that deviate from forming a straigt line are considered endpoints of segments.

FLD is suitable for applications where speed is crucial such as real-time systems or applications where processing resources are limited. The exact implementation details vary based on the specific version of OpenCV and underlying optimizations applied.

4.4.2 Postprocessing

The results of the FLD algorithm are post-processed to incorporate domain specific knowledge. More precisely, we filter out lines based on the observation that cameras with different orientation capture rail tracks that are bounded by boxes of different aspect

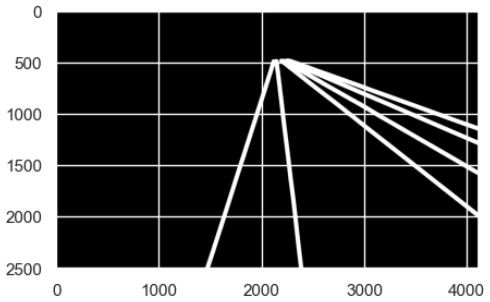

(a) Ground truth label selected randomly from training set.

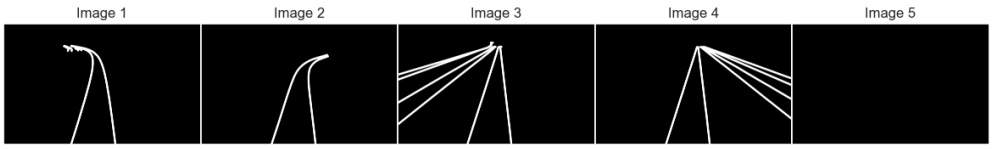

(b) Example predictions selected randomly from training set; last image is only background illustrating a case where no rail track was found

Image	Pixel Accuracy	Precision	Recall	Dice	IoU
1	0.927	0.013	0.005	0.007	0.004
2	0.956	0.706	0.249	0.369	0.226
3	0.916	0.197	0.201	0.199	0.111
4	0.999	0.992	0.991	0.991	0.983
5	0.948	-[a]	0.0	0.0	0.0

[a]Division by zero as there are no positive classifications.

(c) Performance Metrics

Figure 18: Example masks – ground truth vs. prediction.

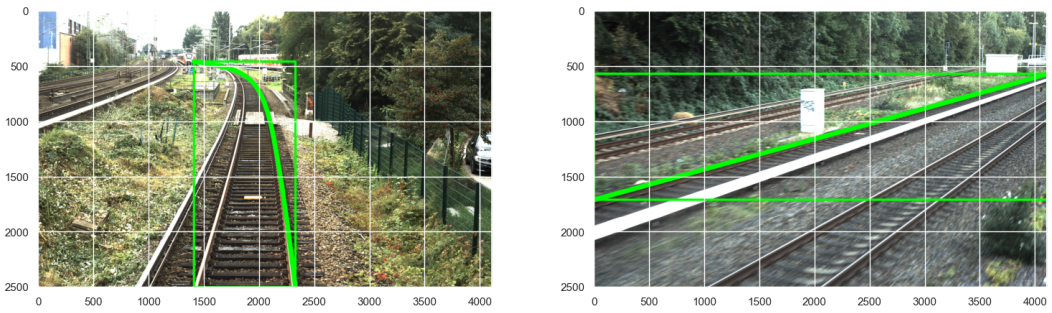

(a) Center camera: elongated bounding box aspect ratio.

(b) Left camera: wide bounding box aspect ratio.

Figure 19: Different bounding box aspect ratios depending on camera orientation.

ratios. Figure 19 illustrate the idea: Figure 19a shows an image of a forward facing camera; the aspect ration of the bounding box enclosing the track is large. Figure 19b shows an image of a left facing camera; the aspect ratio of the bounding box enclosing the track is small.

Figure 20 gives the distribution of the bounding box aspect ratios for the different camera orientations in the OSDaR23 dataset. The histogram confirms the idea that different sensors have different aspect ratios for the bounding boxes. For more details see Appendix A.3.

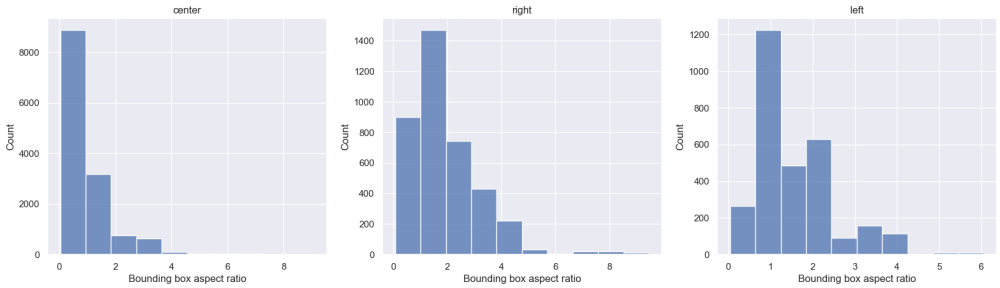

Figure 20: Histogram of bounding box aspect ratios by camera orientation.

The aspect ratios are used to remove all lines detected by FLD that have a bounding box aspect ratio smaller than the x^{th} Quantile or larger than the $1 - x^{th}$ Quantile.

In a final step, we apply Connected Component Labeling (CCL) to remove noise or segments that are false positives (OpenCV, 2024a). The goals of CCL is to identify and label connected regions in a binary image where pixels are either tracks or background. After connected components are labeled in the image, we remove all components that are x% smaller than the largest component.

The entire process is illustrated in Figure 21. The final result showcases that the approach is a heuristic that filters out true positive labels.

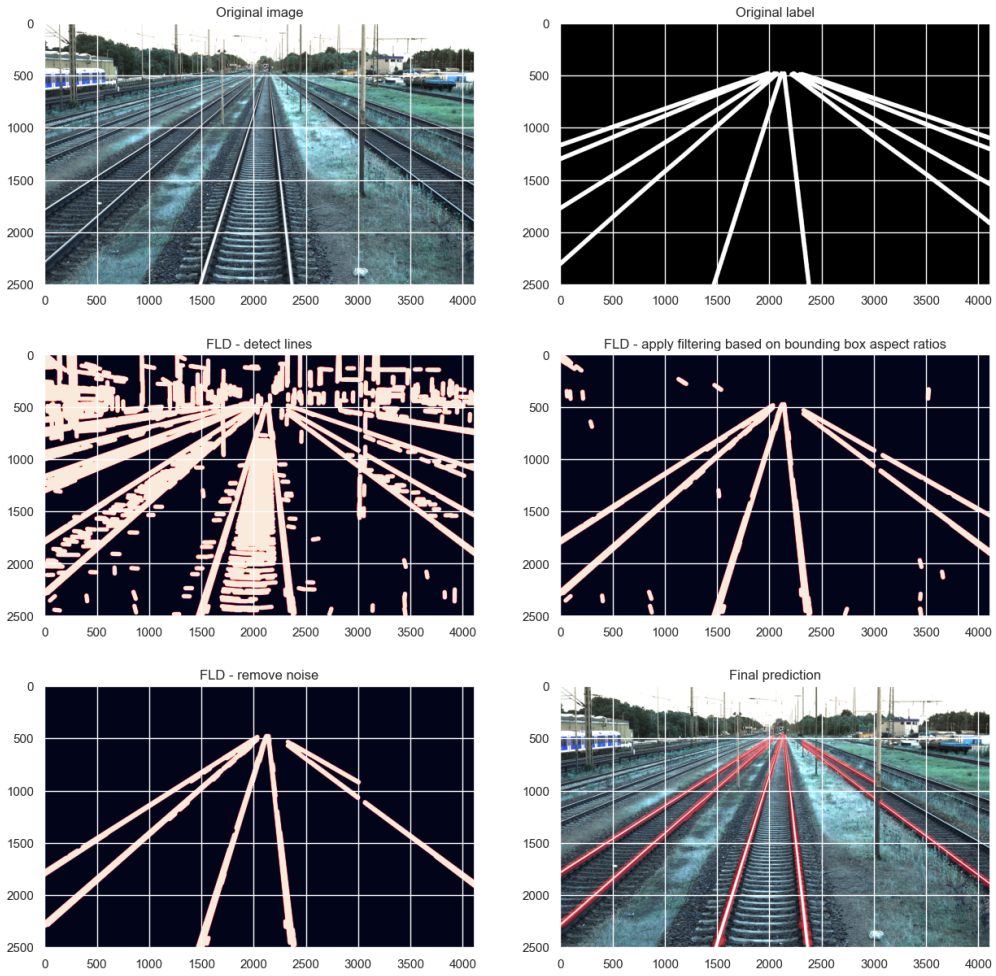

Figure 21: Baselining approach based on fast line detection and post-processing.

4.4.3 Parameter tuning

The performance of our traditional rail detection algorithm depends on a number of parameters. In order to choose the best parameter setting for each combination of sensor and orientation, we tune the parameters according to the grid search technique. Grid search involves specifying a grid of parameter values and exhaustively evaluating the performance of the algorithm for each combination of values. The parameter combination that yields the best performance is selected. Grid search is a simple technique that

thoroughly explores the parameter space but it is also computationally expensive in multi-dimensional spaces.

In total, we test 22.680 parameter settings on 196 images[1] from the Os dataset. The images are sampled randomly from the train set such that there is at most one image per sensor per video sequence.

Table 2: Sensor Parameters

Parameter	**Description**	**Values**
Sensors	Combination of sensor and orientation	rgb_highres_left, rgb_highres_right, rgb_highres_center, rgb_left, rgb_right, rgb_center, ir_left, ir_right, ir_center ir_left, ir_right, ir_center
Kernel	Kernel for Gaussian blur	0, 3, 5, 7
Length Threshold	Segment shorter than this will be discarded	25, 50, 100, 200, 300
Canny Threshold 1	First threshold for hysteresis procedure in Canny; second threshold is threshold 1 times 3	5, 10, 20, 50, 100, 150
Aspect Ratio Quantile	Filtering out lines with depending on bounding box aspect ratio quantile	1, 5, 10
Noise Threshold	Removing small segments that are classified as noise	0.0, 0.05, 0.1, 0.15, 0.2, 0.25, 0.3

Table 3 presents the best parameter configurations based on the average Dice score. The varying parameter settings across different sensors demonstrates the algorithm's sensitivity to the selected parameters. The left-oriented camera images seem to benefit from a higher level of blurring with a kernel size of seven. The filtering criteria for lines with uncharacteristic bounding box aspect ratios appear to be relatively loose in most cases – only the most extreme outliers are being removed. Left and right-oriented high-resolution camera images, on the other hand, seem require a more restrictive filtering. The "Avg. Time" column indicates the average inference time in seconds. The inference times seem to be strongly correlated with the entropy metrics discussed in Section 3.1.3; higher entropy values tend to be associated with longer inference times.

4.5 Deep-learning based segmentation

In this section, we will describe the deep-learning based segmentation in more detail. The applied model is YOLOv8 which is the latest version of YOLO models by Jocher et al. (2023). YOLOv8 is distributed under the GNU General Public License, which authorizes the users to freely share, modify and distribute the software. The accessibility of the

[1] The idea is to select one image for each combination of sensor, sensor orientation, and video sequence in the train set (i.e., $3 \times 3 \times 33 = 297$). However, there are combinations with no track labels.

Sensor	Kernel	Length Threshold	Aspect Ratio Quantile	Canny Th1	Canny Th2	Noise Threshold	Avg. Time (sec)
rgb_highres_center	5	50	1	50	150	0.25	0.052
rgb_highres_right	0	100	5	10	30	0.25	0.074
rgb_center	3	100	1	10	30	0.2	0.014
rgb_highres_left	7	50	5	50	150	0.25	0.069
rgb_right	3	50	1	5	15	0.1	0.032
ir_left	7	25	1	5	15	0.2	0.003
rgb_left	7	100	1	20	60	0.25	0.026
ir_center	3	25	1	5	15	0.2	0.003
ir_right	5	25	1	10	30	0.2	0.004

Table 3: Best parameter settings and associated performance metrics.

code as well as high performance on many applications led to a large community and much resources for developing and tuning YOLO models.

YOLOv8 is used to detect objects in images with a single forward pass through the network. The models are pre-trained on large datasets like COCO and ImageNet which enables the prediction of everyday objects (Krishnakumar, 2023). Additionally, in line with the transfer learning technique, the model can be fine-tuned on new datasets related to the problem at hand (i.e., rail track detection). The model architecture is presented in Appendix A.4. YOLOv8-Seg model is an extension of the YOLOv8 object detection model that performs semantic segmentation of the input image. The model has been shown to achieve state-of-the-art results on a variety of object detection and semantic segmentation benchmarks while maintaining high speed and efficiency (Krishnakumar, 2023).

YOLOv8-seg uses a weighted loss function comprising bounding box loss, objectness loss, and segmentation loss (Jocher, 2023). Bounding box loss calculates the error between the geometry of the predicted and the ground truth box. It is a measure of how well the model predicts the size and location of the bounding boxes. Objectness loss determines how confident the model is about the presence of an object in the bounding box. It compares the probability of an object being present in the prediction with the ground truth value. Finally, segmentation loss quantifies how close the predicted segmentation map is to the ground truth map. It measures how effectively the model performs the semantic segmentation task.

4.5.1 Models

In order to identify the best model setup for the rail track detection task, we experiment with 18 different models that are validated against different datasets. The models differ in the data the model is trained on, the size of the input image, and the labeling approach. All models are trained for 300 epochs. However, the optimization process stops if there has been no improvement in the last 50 epochs. Hyper-parameters are either set to default values or automatically chosen in the initialization phase by YOLO.

Table 4 summarizes the setup of the different models. The “Epochs” column gives the actual number of epochs and “Duration” is the wall-clock time for the training process with unified labels and separate labels, respectively. The remaining specifications in the table are the regardless of the labeling approach. The column “Train Set” gives the set of images that are used to train the model. “Image Size” is either set to 640 or 1280 in order to assess the influence of the image size in the prediction results; the model resizes the input image such that the larger dimension scaled to 640 pixels while maintaining the original aspect ratio (e.g., the RGB low resolution images are resized from 2464x1600 to 640x416 as the image length and width have to be a multiples of 32). The batch size is selected automatically by YOLO such that the model can best utilize the available GPU memory without running into “out of memory” situations. The “Optimizer” column gives the optimization algorithms used for training the neural networks. The optimizer is selected automatically. SGD (Stochastic Gradient Descent) is a basic optimization algorithm used to minimize the loss function during the training of neural networks. In each iteration, SGD randomly selects a subset of training examples (also referred to as mini-batch) to compute the gradient estimate which supports faster convergence (Bottou, 2010). AdamW (Adam with Weight Decay) is a variant of the Adam optimizer that includes an additional term for weight decay regularization. AdamW combines the advantages of both Adam and weight decay regularization which helps prevent overfitting by penalizing large parameter values (Kingma and Ba, 2014).

When looking at the table, it becomes apparent that the size of the input images has a large impact on the batch size. With images of size 640×640 23 images can be processed per iteration. If the images have 1280×1280 pixels, only 5 images can be processed at once with the given computational resources (i.e., GPU memory). The automatic selection of optimizers seems to depend on whether or not the Railsem19 images are added to the train set. With Railsem19 data YOLO selects the SGD optimizer, without Railsem19 data the AdamW optimizer is used. In terms of computational time, it appears that the high-resolution images significantly influence the duration of processing.

Train Set	Image Size	Batch Size	Optimizer	Unified labels		Separate labels	
				Epochs	Duration (HH:MM:SS)	Epoch	Duration (HH:MM:SS)
OSDaR23 RGB	640	23	AdamW	121	00:37:57	93	00:35:29
OSDaR23 infrared	640	23	AdamW	196	00:51:51	223	01:01:10
OSDaR23 RGB	1280	5	AdamW	117	01:39:58	247	03:54:41
OSDaR23 RGB + Railsem19	640	23	SGD	138	02:44:37	300	08:45:13
OSDaR23 high-res	1280	5	AdamW	81	04:20:46	119	17:36:20
OSDaR23 high-res + Railsem19	640	23	SGD	110	13:36:26	300	60:03:41
OSDaR23 high-res	640	23	AdamW	130	13:53:44	285	43:27:41
All OSDaR23	640	23	SGD	189	23:27:11	172	36:45:33
All OSDaR23 + Railsem19	640	23	SGD	224	23:42:53	300	64:51:24

Table 4: Training details

Among the experiments with 640×640 images, the presence of high-resolution images in the training set causes at least a five-fold increase in the computation time per epoch. The labeling approach is another factor that has a large effect on the computational time; training the model with all images (OSDaR23 and RailSem19) with separate labels took almost three days whereas with unified labels the training stopped after less than a day. Also all models with unified labels stopped early as no improvement was observed for 50 epochs. With separate labels the maximum number of iterations was reached in models that incorporated the RailSem19 dataset.

Figure 30, presents the results of the experiments with unified labels on the left and with separate labels on the right. On the y-axis, we list the nine models introduced above. The x-axis shows the validation sets on which the models are tested. The models are compared based on the average Dice score.

The model that performs best on all OSDaR23 images is data_all_railsem_640, on OSDaR23 high-resolution images data_highres_railsem_640, on OSDaR23 infrared images data_all_640 with unified labels and data_all_railsem_640 with separate labels, and on OSDaR23 regular RGB images data_highres_railsem_640. This means that all models benefited from adding images from the Railsem19 dataset to the training set, except when applied to the infrared images with unified labels. This outcome comes at no surprise as the Railsem19 dataset comprises a large variety of different images and deep-learning models are known to perform better with more training data. The lack of generalization of the models trained exclusively on the OSDaR23 data becomes apparent when validated against the Railsem19 dataset: the best dice score is 0.35 with the data_all_640 model compared to 0.76 with the data_highres_railsem_640 model when labels are unified; with separate labels the difference is 0.44 versus 0.71. It is also interesting to observe the models trained on and validated against infrared images. While

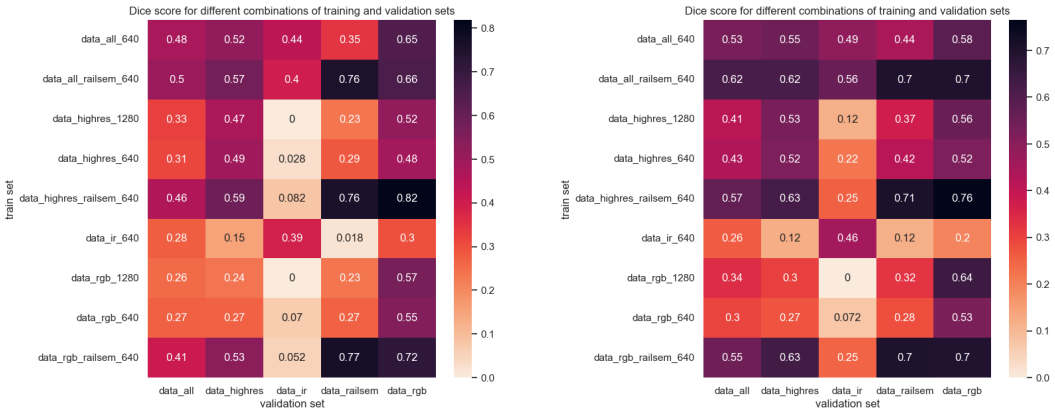

(a) Models with unified labels.

(b) Models with separate labels.

Figure 22: Models with different train and validation set.

all models with unified labels fail to predict tracks in infrared images except of models that are trained on infrared images, models trained on infrared images exclusively can predict tracks in RGB images with a Dice score of 0.3. This indicates that training on infrared images support the prediction on RGB images but not the other way round. The picture is different when each track is labeled separately. Even if the training set does not contain infrared images, track can be predicted in infrared images with a dice score of 0.25.

In general, the results clearly indicate that the performance of the segmentation approach depends on the availability of appropriate training data. The comparison between the different labeling approaches is not straight forward because the dice score is calculated differently. We will perform a comparison based on the same metrics in Section **??**.

The comparison between using 1200 pixel images as input and 600 pixel images reveals that using larger images has no clear advantage on the solution quality. In certain cases (e.g., data_railsem) the Dice score even decrease when using 1280 images rather than 640 pixel images which might be caused by the smaller batch size that fits into the memory in each training step. What is more, using larger images considerably increases the inference speed which might become a bottle-neck in real-life applications. Table 5 show that using large images as input can increase the average inference speed by a factor of around 4.

Going forward, we will focus on the models data_highres_railsem_640 and data_all_640 with unified labels, and models data_highres_railsem_640 and

Train Set	Inference speed unified labels [ms]		Inference speed separate labels [ms]	
	data_highres	**data_rgb**	**data_highres**	**data_rgb**
data_highres_1280	7.286	7.478	10.768	11.624
data_highres_640	1.696	1.745	4.138	3.001
data_rgb_1280	5.371	6.755	8.306	8.869
data_rgb_640	2.019	1.867	1.716	1.931

Table 5: Inference speed in milliseconds

data_all_railsem_640 with separate labels for further analysis and refinement as these models provided the best results on the OSDaR23 validation sets. The detailed training results are given in Appending A.4.

4.5.2 Parameter tuning

Parameter tuning or hyperparameter tuning refers to the process of selecting the optimal hyperparameters for a neural network model. Hyperparameters cannot be directly learned from the training data but are high-level settings that are provided as an external input to the model. The goal of parameter tuning is to find the combination of hyperparameters that results in the best performance. Ultralytics YOLO uses genetic algorithms to optimize hyperparameters. Genetic algorithms are inspired by the mechanism of natural selection and genetics based on, e.g., mutation (Inc., 2023).

Parameter tuning is an iterative process where in each iteration the fitness of the current setting is assessed by training the model for a given number of epochs. We set the number of iterations to 300 and the number of epochs per iteration to 30. Preliminary experiments revealed that the tuning process is computationally expensive. Therefore, the tuning is performed on 10% of the training data. Table 6 summarizes the tuning runs with unified labels. The tuning is very resource intensive despite the reduced training set. The tuning on the high-resolution OSDaR23 images plus Railsem19 images took at 146 hours with the SGD optimizer and could not be finished within 148 hours with the AdamW optimizer.

Table 7 compare the results with unified labels that are generated by automatically setting the parameters by YOLO, tuning with SGD, and tuning with AdamW. The data_all_640 model is used for the infrared images and data_highres_railsem_640 model is used for the RGB images. The results indicate that the automatically chosen parameters outperform the tuned parameters on two out of four tests. This is a surprising

Model	Optimizer	Duration [h]
data_highres_railsem_640	AdamW	148[a]
	SGD	146
data_all_640	AdamW	50
	SGD	51

[a]Tuning run was aborted by the system after 160 iterations.

Table 6: Parameter tuning with unified labels.

result but it can probably be explained by the reduced training set that was used during the parameter tuning. For example, if the subset of the training data used for tuning contained less infrared images relative to the entire training set, then the parameters of the data_all_640 model would be tuned towards performing better on RGB images. Detailed results of the tuning are given in Appendix A.4.5.

Given the good overall performance of the automatically tuned parameters and the poor performance of the tuned parameters on the data_rgb set, we use the models with the automatically chosen parameters for the final analysis. The parameter tuning was omitted for the models with separate labels due to the poor cost/benefit ratio.

Model	Validation Set	Dice			SGD vs. AdamW	AdamW
		Auto	Tuned SGD	Tuned AdamW	Auto [%]	Auto [%]
data_all_640	data_ir	**0.440**	0.425	0.375	-3.324	-14.704
data_highres_railsem_640	data_highres	0.587	**0.596**	0.558	1.480	-4.913
	data_railsem	0.758	0.765	**0.766**	0.879	1.057
	data_rgb	**0.818**	0.774	0.752	-5.440	-8.140

Table 7: Comparison of automatically chosen parameters and tuned parameters based on Dice score with unified labels.

5 Results

In this section, we perform a detailed analysis of the proposed solution approaches on the test set. The test set was not used during the model development and training process, so the results provide an unbiased performance evaluation on unseen data. Both approaches, FLD and YOLOv8, are used to predict tracks in the test images. The evaluation is based on the Dice score.

COMPARE BOTH YOLO models!!!!!!!!!!!!!!!!!!!!!!!!!

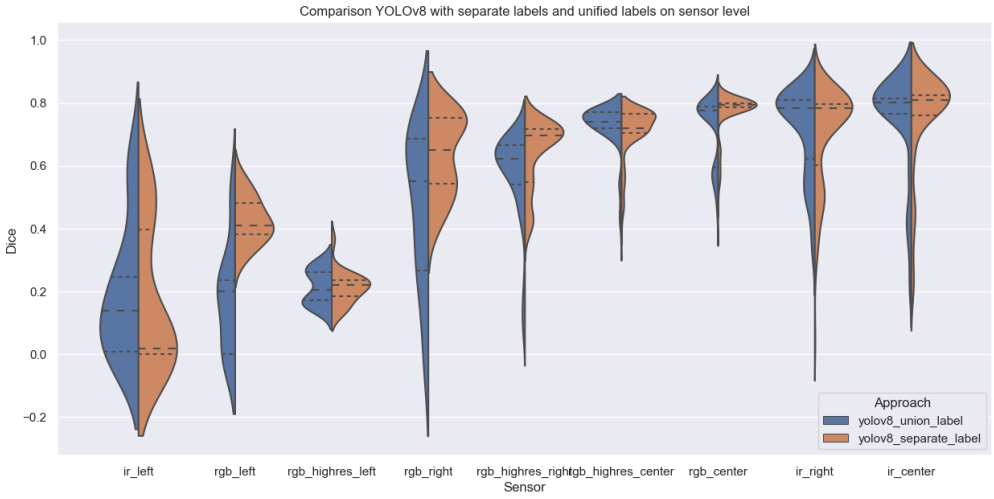

Figure 23: Comparison between YOLOv8 models with unified label and separate labels by sensor type.

In Figure 25, shows the comparison between FLD and YOLOv8 based on the Dice score where each data point represents one image. The sensor types are distinguished by color. The dashed red line represents the indifference line, where points along this line signify that both, YOLOv8 and FLD solutions, are equal good or bad. If a points is above the line then YOLOv8 performed better on that image; if a point is below the line FLD outperformed YOLOv8. It is easy to see that YOLOv8 outperforms FLD on most images. However, it is interesting to observe that on certain RGB images FLD provides predictions with a Dice score of up to 0.37. A closer look reveals that all images where YOLOv8 could not provide a prediction are frames from the same sequence. An example is given in Figure 26; predictions are colored red. Similarly, the cluster of high-resolution images on which FLD performs better are all frames from the same sequence. The prediction of YOLOv8 and of FLD on one of these frames is given in Figure 26 An other

(a) Prediction image with unified labels.

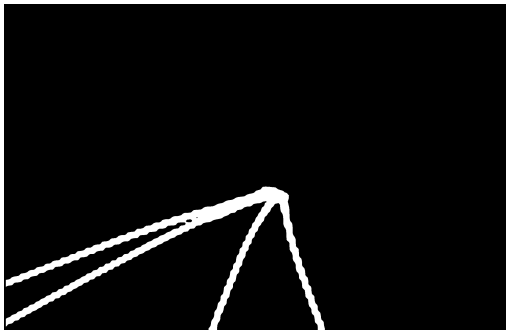

(b) Prediction mask with unified labels.

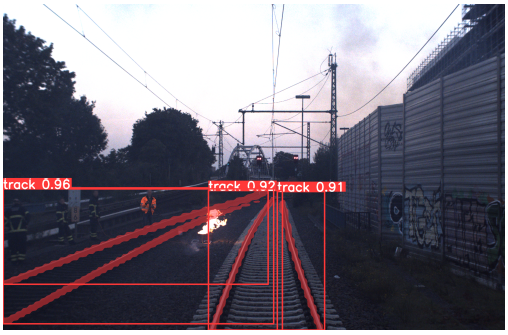

(c) Prediction image with separate labels.

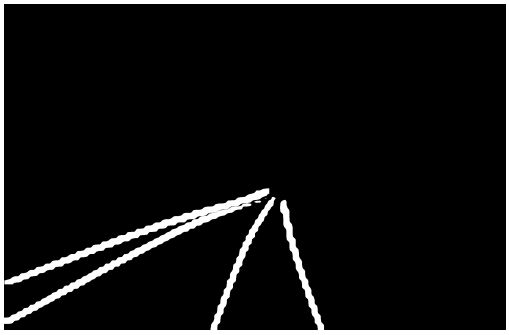

(d) Prediction mask with separate labels.

Figure 24: Example results of different labeling approaches.

interesting observation is that infrared images have the highest Dice scores among the images segmented with YOLOv8. Figure 28 illustrates the difference between FLD and YOLOv8 on an infrared image.

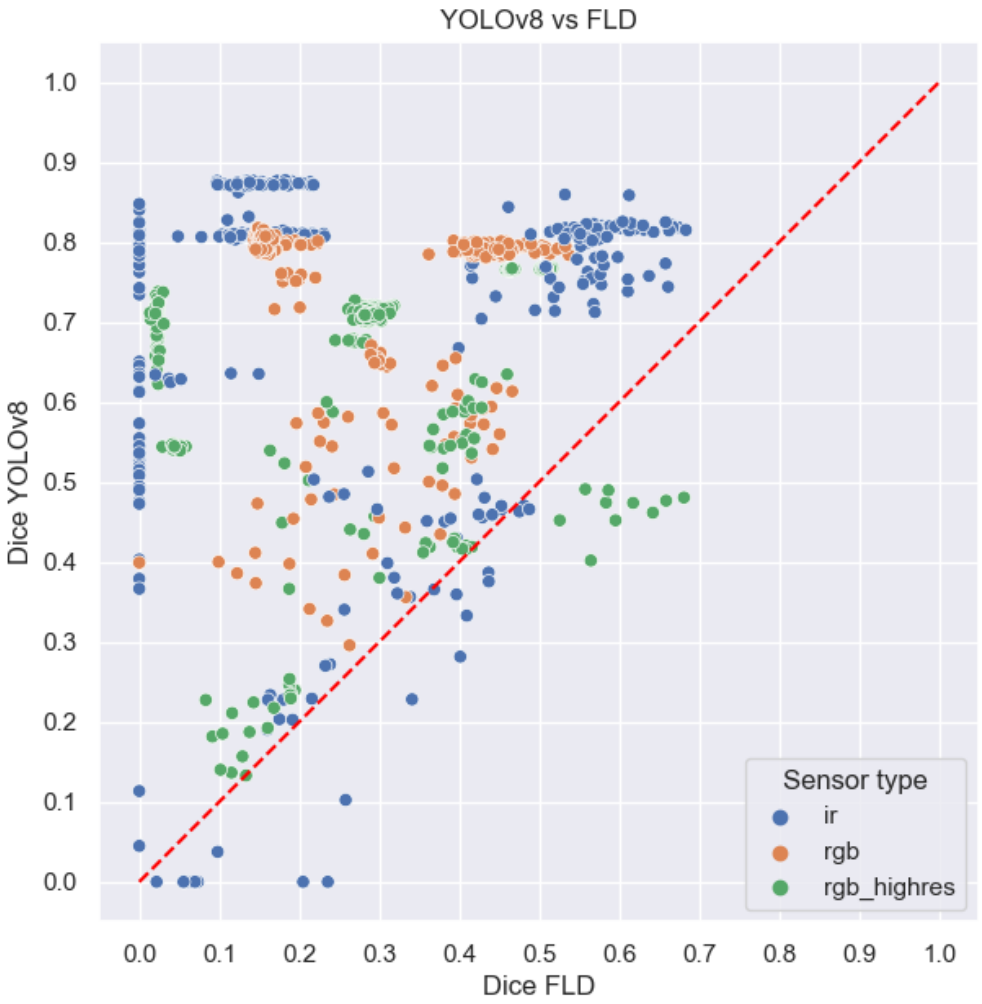

Figure 25: Comparison between YOLOv8 (separate labels) and FLD based on Dice score. Sensor types are distinguished by color.

In Section 4.4.3, we have seen that the image entropy has an effect on the computation time. Next, in Figure 29, we examine the relation between Dice and entropy score; the different approaches are distinguished by color. There is no clear trend in the scatter plot, i.e., there is no linear relationship between Dice score and entropy. However, both approaches seem to struggle with low entropy images that have uniform intensity (e.g., which is often the case with infrared images – see Figure 8a).

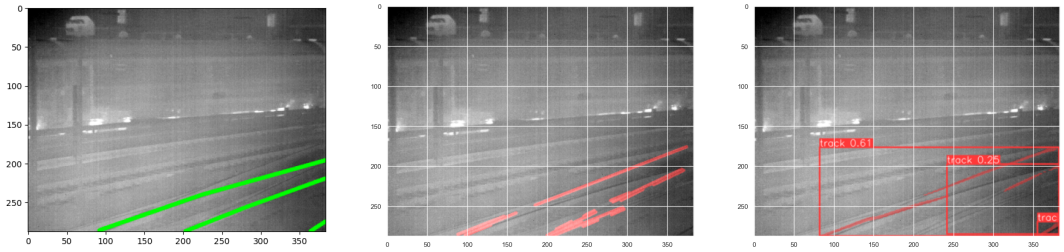

(a) Image with ground truth label in green.

(b) FLD provides better prediction for main tracks; the side tracks are only partially segmented.

(c) YOLOv8 has many False Negative pixels and low confidence in the result (confidence values are given for each bounding box).

Figure 26: Example image where FLD performs better than YOLOv8; predictions are colored red.

(a) Image with ground truth label in green.

(b) FLD provides good prediction for main tracks; the side tracks are only partially segmented.

(c) YOLOv8 has many False Negative pixels – confidence values are given for each bounding box.

Figure 27: Example where FLD slightly outperforms YOLOv8.

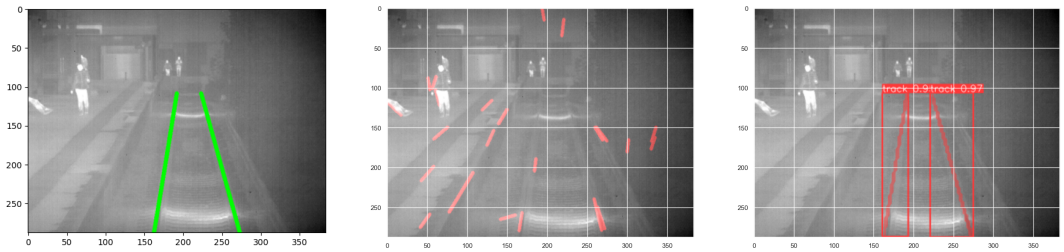

(a) Image with ground truth label in green.

(b) FLD approach cannot detect tracks efficiently in the example image.

(c) YOLOv8 provides precise segmentation with high confidence.

Figure 28: Extreme example where YOLOv8 clearly outperforms FLD.

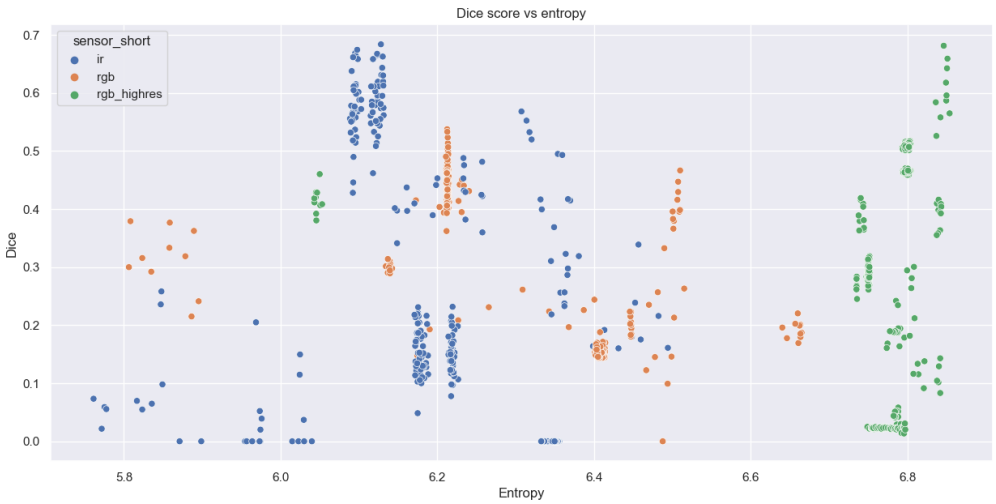

Figure 29: Dice scores vs. entropy scores – FLD and YOLOv8 are distinguished by color.

Figure 30, evaluates and compares FLD and YOLOv8 on sensor level. The dice scores are visualized in a violin plot that combines aspects of a box plot and a kernel density plot. The Figure supports the conclusion from Figure 25: YOLOv8 performs better than FLD in most of the cases. YOLOv8 performs particularly well on infrared images. Good results are achieved with forward-facing sensors. In particular, FLD performs best on forward-facing RGB cameras but performs poorly when the cameras are left or right oriented. YOLOv8 is more robust to the sensor type and orientation. Segmenting tracks on images of left oriented cameras seems to be particularly challenging. This might be an outcome of the right-hand traffic principle which is mostly followed in Germany.

5.1 Post-processing and application

6 Conclusion

This master's thesis addresses a challenge in the area of railway automation. The focus is on multi-sensor rail track detection within the context of Automatic Train Operations (ATO). Leveraging deep learning techniques, particularly semantic segmentation, the

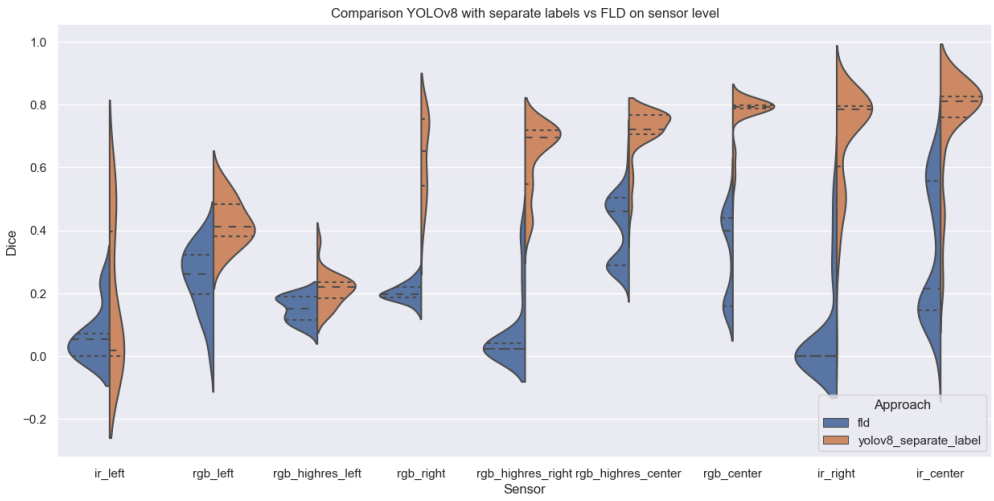

Figure 30: Violin plot indicating the difference between YOLOv8 and FLD on sensor level.

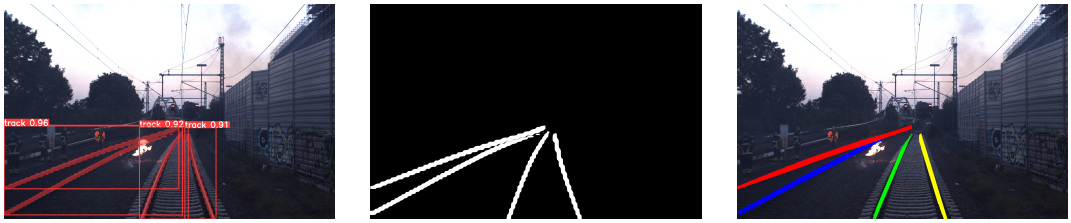

(a) Segmented image. (b) Segmentation mask comprising four tracks. (c) Each track can be identified separately.

Figure 31: Lines.

study aims to enhance the accuracy and robustness of track detection systems thereby contributing to the efficiency and safety of railway operations.

The research compares deep learning-based segmentation with traditional non-AI-based methods, exploring the effectiveness of different sensor inputs and orientations. By conducting a comprehensive performance evaluation and integrating the developed model into real-world applications, valuable insights are gained into the feasibility and practical implications of automated track detection systems.

The results demonstrate the advantages of deep learning-based approaches, particularly YOLOv8, over traditional methods in most scenarios. YOLOv8 performs robustly across various sensor types and orientations, with infrared images yielding the highest Dice scores. Furthermore, the highlights the challenges associated with low entropy images and the impact of sensor orientation on segmentation accuracy.

Overall, this research advances the field of railway automation by providing valuable insights, methodologies, and tools for improving the safety, efficiency, and competitiveness of automatic train operations. The findings hold significant implications for railway infrastructure management and contribute to the ongoing efforts towards sustainable transportation systems.

Future research could involve applying other deep-learning techniques instead of semantic segmentation. Give the fact that desired output are polylines marking tracks, it would be interesting to adjust the YOLinO approach proposed by Meyer et al. (2021) for lane detection. Furthermore, distinguishing the tracks the locomotive occupies currently from the surrounding tracks would support the navigation in the network. The devised approach performs well on images from infrared sensors. Therefore, research could focus on more detailed analysis on track detection in adverse weather and low lighting conditions.

Bibliography

Emilio J. Almazàn, Ron Tal, Yiming Qian, and James H. Elder. Mcmlsd: A dynamic programming approach to line segment detection. In *2017 IEEE Conference on Computer Vision and Pattern Recognition (CVPR)*, pages 5854–5862, 2017. doi: 10.1109/CVPR.2017.620.

ALSTOM Transport SA. Autonomous mobility: The future of rail is automated, 2021. URL https://www.alstom.com/autonomous-mobility-future-rail-automated.

Mostafa Arastounia. Automated recognition of railroad infrastructure in rural areas from lidar data. *Remote Sensing*, 7(11):14916–14938, 2015. ISSN 2072-4292. doi: 10.3390/rs71114916. URL https://www.mdpi.com/2072-4292/7/11/14916.

Léon Bottou. Large-scale machine learning with stochastic gradient descent. In *Proceedings of COMPSTAT'2010: 19th International Conference on Computational StatisticsParis France, August 22-27, 2010 Keynote, Invited and Contributed Papers*, pages 177–186. Springer, 2010.

Jieren Cheng, Hua Li, Dengbo Li, Shuai Hua, and Victor S. Sheng. A survey on image semantic segmentation using deep learning techniques. *Computers, Materials & Continua*, 74(1):1941–1957, 2023. ISSN 1546-2226. doi: 10.32604/cmc.2023.032757. URL http://www.techscience.com/cmc/v74n1/49879.

M Clark, D.M McCann, and M.C Forde. Infrared thermographic investigation of railway track ballast. *NDT & E International*, 35(2):83–94, 2002. ISSN 0963-8695. doi: https://doi.org/10.1016/S0963-8695(01)00032-9. URL https://www.sciencedirect.com/science/article/pii/S0963869501000329.

Deutsche Bahn AG. Automatic train operation (ato), 2022. URL https://digitale-schiene-deutschland.de/en/Automatic-Train-Operation.

Deutsche Bahn AG. First freely available multi-sensor data set for machine learning for the development of fully automated driving: Osdar23, 2023. URL https://digitale-schiene-deutschland.de/en/news/2023/OSDaR23-multi-sensor-data-set-for-machine-learning.

Tausif Diwan, G. Anirudh, and Jitendra V. Tembhurne. Object detection using yolo: challenges, architectural successors, datasets and applications. *Multimedia Tools and Applications*, 82(6):9243–9275, 03 2023. ISSN 1573-7721. doi: 10.1007/s11042-022-13644-y. URL https://doi.org/10.1007/s11042-022-13644-y.

Richard O. Duda and Peter E. Hart. Use of the hough transformation to detect lines and curves in pictures. *Commun. ACM*, 15(1):11–15, jan 1972. ISSN 0001-0782. doi: 10.1145/361237.361242. URL https://doi.org/10.1145/361237.361242.

Europe's Rail Joint Undertaking. Innovation in the spotlight: Towards unattended mainline train operations (ato goa 4), 2019. URL https://rail-research.europa.eu/highlight/innovation-in-the-spotlight-towards-unattended-mainline-train-operations-ato-goa4/.

Haogang Feng, Gaoze Mu, Shida Zhong, Peichang Zhang, and Tao Yuan. Benchmark analysis of yolo performance on edge intelligence devices. *Cryptography*, 6(2), 2022. ISSN 2410-387X. doi: 10.3390/cryptography6020016. URL https://www.mdpi.com/2410-387X/6/2/16.

Xavier Giben, Vishal M. Patel, and Rama Chellappa. Material classification and semantic segmentation of railway track images with deep convolutional neural networks. In *2015 IEEE International Conference on Image Processing (ICIP)*, pages 621–625, 2015. doi: 10.1109/ICIP.2015.7350873.

Rafael Grompone von Gioi, Jeremie Jakubowicz, Jean-Michel Morel, and Gregory Randall. Lsd: A fast line segment detector with a false detection control. *IEEE Transactions on Pattern Analysis and Machine Intelligence*, 32(4):722–732, 2010. doi: 10.1109/TPAMI.2008.300.

Rafael Grompone von Gioi, Jérémie Jakubowicz, Jean-Michel Morel, and Gregory Randall. LSD: a Line Segment Detector. *Image Processing On Line*, 2:35–55, 2012. https://doi.org/10.5201/ipol.2012.gjmr-lsd.

Ultralytics Inc. Ultralytics YOLO Hyperparameter Tuning Guide, 2023. URL https://docs.ultralytics.com//guides/hyperparameter-tuning/#train-model.

International Energy Agency. The future of rail, 2019. URL https://www.iea.org/reports/the-future-of-rail.

Dewan Md Zahurul Islam, Stefano Ricci, and Bo-Lennart Nelldal. How to make modal shift from road to rail possible in the european transport market, as aspired to in the eu transport white paper 2011. *European transport research review*, 8(3):1–14, 2016.

Peiyuan Jiang, Daji Ergu, Fangyao Liu, Ying Cai, and Bo Ma. A review of yolo algorithm developments. *Procedia Computer Science*, 199:1066–1073, 2022. ISSN 1877-0509. doi: https://doi.org/10.1016/j.procs.2022.01.135. URL https://www.sciencedirect.com/science/article/pii/S1877050922001363. The 8th International Conference on Information Technology and Quantitative Management (ITQM 2020 & 2021): Developing Global Digital Economy after COVID-19.

Glenn Jocher. What is the loss used for YOLOv8-seg?, 2023. URL https://github.com/ultralytics/ultralytics/issues/3882.

Glenn Jocher, Ayush Chaurasia, and Jing Qiu. Ultralytics YOLO. https://github.com/ultralytics/ultralytics, January 2023. AGPL-3.0 License.

Fatih Kaleli and Yusuf Sinan Akgul. Vision-based railroad track extraction using dynamic programming. In *2009 12th International IEEE Conference on Intelligent Transportation Systems*, pages 1–6, 2009. doi: 10.1109/ITSC.2009.5309526.

Diederik P Kingma and Jimmy Ba. Adam: A method for stochastic optimization. *arXiv preprint arXiv:1412.6980*, 2014.

Mukilan Krishnakumar. A Gentle Introduction to YOLOv8, 2023. URL https://wandb.ai/mukilan/wildlife-yolov8/reports/A-Gentle-Introduction-to-YOLOv8--Vmlldzo0MDU5NDA2.

B. Le Saux, A. Beaupère, A. Boulch, J. Brossard, A. Manier, and G. Villemin. Railway detection: From filtering to segmentation networks. In *IGARSS 2018 - 2018 IEEE International Geoscience and Remote Sensing Symposium*, pages 4819–4822, 2018. doi: 10.1109/IGARSS.2018.8517865.

Xinpeng Li and Xiaojiang Peng. Rail detection: An efficient row-based network and a new benchmark. In *Proceedings of the 30th ACM International Conference on Multimedia*, MM '22, page 6455–6463, New York, NY, USA, 2022. Association for Computing Machinery. ISBN 9781450392037. doi: 10.1145/3503161.3548050. URL https://doi.org/10.1145/3503161.3548050.

Chao Ma and Mei Xie. A method for lane detection based on color clustering. In *2010 Third International Conference on Knowledge Discovery and Data Mining*, pages 200–203, 2010. doi: 10.1109/WKDD.2010.118.

Annika Meyer, Philipp Skudlik, Jan-Hendrik Pauls, and Christoph Stiller. Yolino: Generic single shot polyline detection in real time. In *Proceedings of the IEEE/CVF International Conference on Computer Vision*, pages 2916–2925, 2021.

Himanshu Mittal, Avinash Chandra Pandey, Mukesh Saraswat, Sumit Kumar, Raju Pal, and Garv Modwel. A comprehensive survey of image segmentation: clustering methods, performance parameters, and benchmark datasets. *Multimedia Tools and Applications*, 81(24):35001–35026, October 2022. ISSN 1573-7721. doi: 10.1007/s11042-021-10594-9. URL https://doi.org/10.1007/s11042-021-10594-9.

Yujian Mo, Yan Wu, Xinneng Yang, Feilin Liu, and Yujun Liao. Review the state-of-the-art technologies of semantic segmentation based on deep learning. *Neurocomputing*, 493: 626–646, 2022. ISSN 0925-2312. doi: https://doi.org/10.1016/j.neucom.2022.01.005. URL https://www.sciencedirect.com/science/article/pii/S0925231222000054.

Bogdan Tomoyuki Nassu and Masato Ukai. Rail extraction for driver support in railways. In *2011 IEEE Intelligent Vehicles Symposium (IV)*, pages 83–88, 2011. doi: 10.1109/IVS.2011.5940410.

OpenCV. Structural analysis and shape descriptors, 2024a. URL https://docs.opencv.org/3.4/d3/dc0/group__imgproc__shape.html#ga107a78bf7cd25dec05fb4dfc5c9e765f.

OpenCV. Fast line detector, 2024b. URL https://docs.opencv.org/4.x/df/ded/group__ximgproc__fast__line__detector.html.

I Pagand, C Carr, and J Doppelbauer. Fostering the railway sector through the european green deal. *European Union Agency For Railways*, 2020.

Xingang Pan, Jianping Shi, Ping Luo, Xiaogang Wang, and Xiaoou Tang. Spatial as deep: Spatial cnn for traffic scene understanding. In *AAAI Conference on Artificial Intelligence (AAAI)*, February 2018.

Andrei I. Purica, Beatrice Pesquet-Popescu, and Frederic Dufaux. A railroad detection algorithm for infrastructure surveillance using enduring airborne systems. In *2017 IEEE International Conference on Acoustics, Speech and Signal Processing (ICASSP)*, pages 2187–2191, 2017. doi: 10.1109/ICASSP.2017.7952544.

Zhiquan Qi, Yingjie Tian, and Yong Shi. Efficient railway tracks detection and turnouts recognition method using hog features. *Neural Computing and Applications*, 23: 245–254, 2013.

Ameet Annasaheb Rahane and Anbumani Subramanian. Measures of complexity for large scale image datasets. In *2020 International Conference on Artificial Intelligence in Information and Communication (ICAIIC)*, pages 282–287. IEEE, 2020.

RangeKing. Model structure of YOLOv8 detection models, 2023. URL https://github.com/ultralytics/ultralytics/issues/189.

Joseph Redmon, Santosh Divvala, Ross Girshick, and Ali Farhadi. You only look once: Unified, real-time object detection. In *Proceedings of the IEEE conference on computer vision and pattern recognition*, pages 779–788, 2016.

P.K Sahoo, S Soltani, and A.K.C Wong. A survey of thresholding techniques. *Computer Vision, Graphics, and Image Processing*, 41(2):233–260, 1988. ISSN 0734-189X. doi: https://doi.org/10.1016/0734-189X(88)90022-9. URL https://www.sciencedirect.com/science/article/pii/0734189X88900229.

C. E. Shannon. A mathematical theory of communication. *The Bell System Technical Journal*, 27(3):379–423, 1948. doi: 10.1002/j.1538-7305.1948.tb01338.x.

Adrian Straker, Stefano Puliti, Johannes Breidenbach, Christoph Kleinn, Grant Pearse, Rasmus Astrup, and Paul Magdon. Instance segmentation of individual tree crowns with yolov5: A comparison of approaches using the forinstance benchmark lidar dataset. *ISPRS Open Journal of Photogrammetry and Remote Sensing*, 9:100045, 2023. ISSN 2667-3932. doi: https://doi.org/10.1016/j.ophoto.2023.100045. URL https://www.sciencedirect.com/science/article/pii/S2667393223000169.

Rustam Tagiew, Martin Köppel, Karsten Schwalbe, Patrick Denzler, Philipp Neumaier, Tobias Klockau, Martin Boekhoff, Pavel Klasek, and Roman Tilly. Osdar23: Open sensor data for rail 2023. *arXiv preprint arXiv:2305.03001*, 2023.

Abdel Aziz Taha and Allan Hanbury. Metrics for evaluating 3d medical image segmentation: analysis, selection, and tool. *BMC Medical Imaging*, 15(1):29, 8 2015. ISSN 1471-2342. doi: 10.1186/s12880-015-0068-x. URL https://doi.org/10.1186/s12880-015-0068-x.

Jigang Tang, Songbin Li, and Peng Liu. A review of lane detection methods based on deep learning. *Pattern Recognition*, 111:107623, 2021.

Zhu Teng, Feng Liu, and Baopeng Zhang. Visual railway detection by superpixel based intracellular decisions. *Multimedia Tools and Applications*, 75:2473–2486, 2016.

Tugce Toprak, Burak Belenlioglu, Burak Aydın, Cuneyt Guzelis, and M. Alper Selver. Conditional weighted ensemble of transferred models for camera based onboard pedestrian detection in railway driver support systems. *IEEE Transactions on Vehicular Technology*, 69(5):5041–5054, 2020. doi: 10.1109/TVT.2020.2983825.

TuSimple. Tusimple, 2017. URL https://github.com/TuSimple/tusimple-benchmark/tree/master/doc/lane_detection.

Ultralytics Inc. Yolov8, 2023. URL https://docs.ultralytics.com/models/yolov8/.

Jinsheng Wang, Yinchao Ma, Shaofei Huang, Tianrui Hui, Fei Wang, Chen Qian, and Tianzhu Zhang. A keypoint-based global association network for lane detection. In *Proceedings of the IEEE/CVF Conference on Computer Vision and Pattern Recognition*, pages 1392–1401, 2022.

Yin Wang, Lide Wang, Yu Hen Hu, and Ji Qiu. Railnet: A segmentation network for railroad detection. *IEEE Access*, 7:143772–143779, 2019. doi: 10.1109/ACCESS.2019.2945633.

Bisheng Yang and Lina Fang. Automated extraction of 3-d railway tracks from mobile laser scanning point clouds. *IEEE Journal of Selected Topics in Applied Earth Observations and Remote Sensing*, 7(12):4750–4761, 2014. doi: 10.1109/JSTARS.2014.2312378.

Mingyue Yang. Lane detection methods survey for automatic driving. In *Journal of Physics: Conference Series*, volume 2547, page 012015. IOP Publishing, 2023.

Xiang Yue, Kai Qi, Xinyi Na, Yang Zhang, Yanhua Liu, and Cuihong Liu. Improved yolov8-seg network for instance segmentation of healthy and diseased tomato plants in the growth stage. *Agriculture*, 13(8), 2023. ISSN 2077-0472. doi: 10.3390/agriculture13081643. URL https://www.mdpi.com/2077-0472/13/8/1643.

Syed Sahil Abbas Zaidi, Mohammad Samar Ansari, Asra Aslam, Nadia Kanwal, Mamoona Asghar, and Brian Lee. A survey of modern deep learning based object detection models. *Digital Signal Processing*, 126:103514, 2022. ISSN 1051-2004. doi: https://doi.org/10.1016/j.dsp.2022.103514. URL https://www.sciencedirect.com/science/article/pii/S1051200422001312.

Oliver Zendel, Markus Murschitz, Marcel Zeilinger, Daniel Steininger, Sara Abbasi, and Csaba Beleznai. Railsem19: A dataset for semantic rail scene understanding. In *2019 IEEE/CVF Conference on Computer Vision and Pattern Recognition Workshops (CVPRW)*, pages 1221–1229, 2019. doi: 10.1109/CVPRW.2019.00161.

Tu Zheng, Yifei Huang, Yang Liu, Wenjian Tang, Zheng Yang, Deng Cai, and Xiaofei He. Clrnet: Cross layer refinement network for lane detection. In *Proceedings of the IEEE/CVF conference on computer vision and pattern recognition*, pages 898–907, 2022.

List of Figures

List of Tables

A Appendix

A.1 Sensors used in OSDaR23

In this thesis, we are focusing on images from the different sensor types.

Three 12MP RGB Cameras	
Type	Teledyne GenieNano 5GigE C4040
Sensor data	RGB images (8 Bit, PNG)
Resolution	4,112 $\times$ 2,504 px
Sampling frequency	10 Hz (synchronized)
Alignment	trident (in driving direction diagonal left, central and diagonal right)
Three 5MP RGB Cameras	
Type	Teledyne GenieNano C2420
Sensor data	RGB images (8 Bit, PNG)
Resolution	2,464 $\times$ 1,600 px
Sampling frequency	10 Hz (synchronized)
Alignment	trident
Three IR Cameras	
Type	Teledyne Calibir DXM640
Sensor data	Grayscale images (8 Bit, PNG)
Resolution	640 $\times$ 480 px
Sampling frequency	10 Hz (synchronized)
Alignment	trident

Table 8: OSDaR23 sensor specifications

A.2 Dataset split

Splitting the OSDaR23 dataset in to train, validation, and test subsets is performed based on video sequences. Table 9 lists the assignment of sequences to the respective

subset. Figure 32 show the split on an image level in total and for each sensor type.

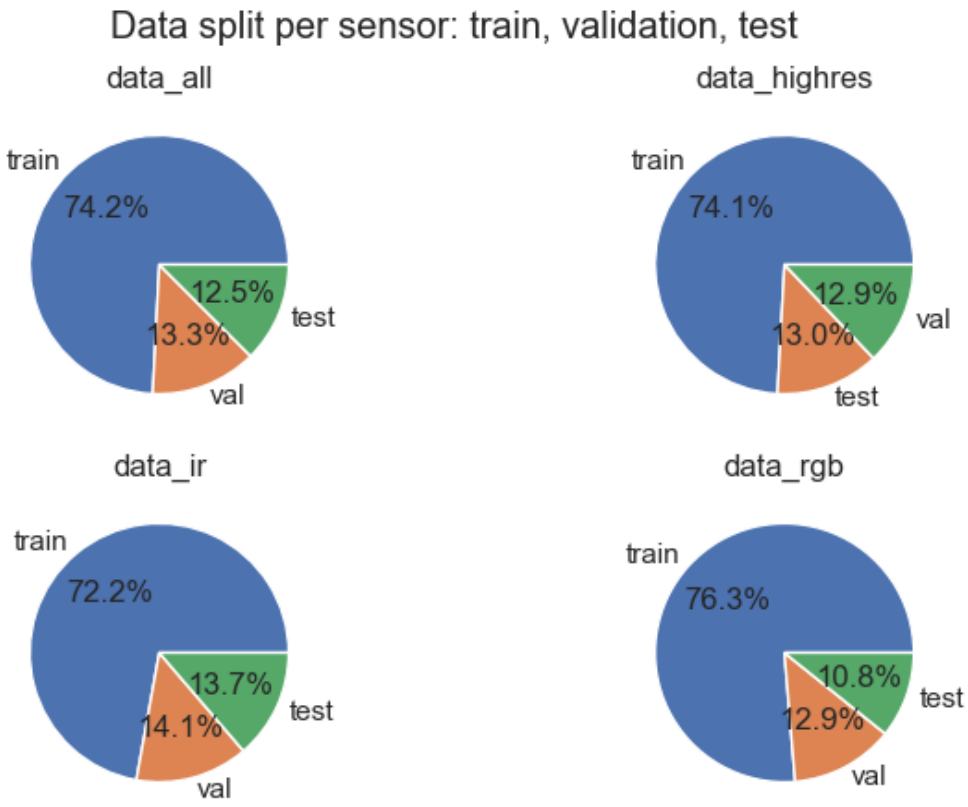

Figure 32: OSDaR23 data split on image level in total and on sensor level.

A.3 Fast line detection

Table 10 gives the statistics of the aspect ratios of bounding boxes enclosing track labels.

Figure 33 shows the effect on the performance measured by the Dice score. The results are averaged over 196 images.

A.4 YOLOv8

Figure 34 presents the model architecture of YOLOv8 (RangeKing, 2023).

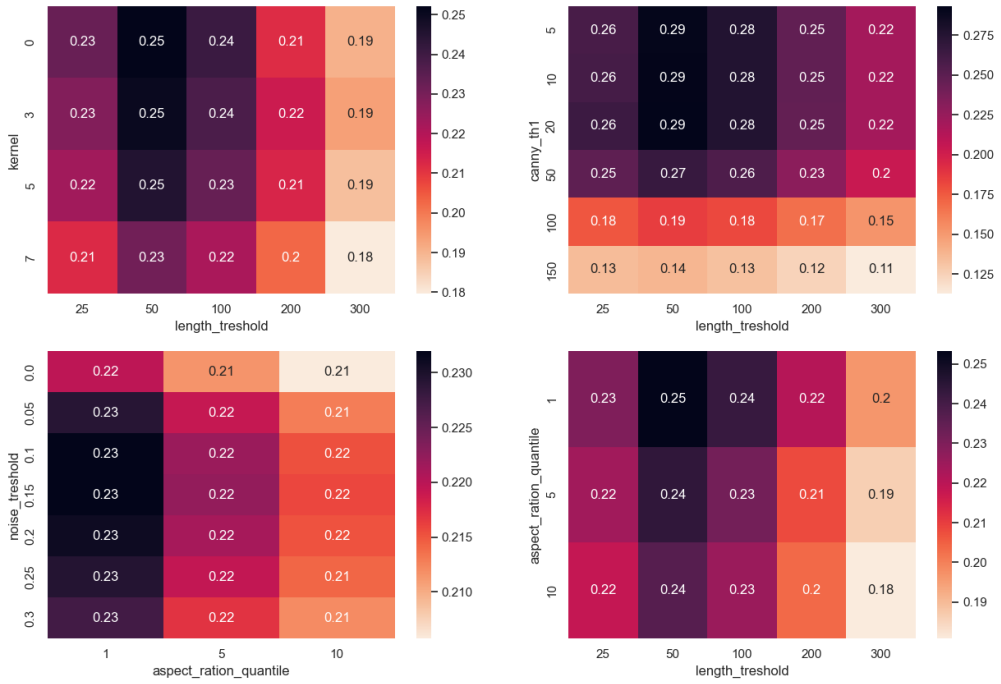

Figure 33: Heatmap of Dice scores for selected parameter pairs. The Dice scores are average values of 196 images.

A.4.1 Results of data_highres_railsem_640 model with unified labels

Figure 35 shows how the performance indicators evolve during the training process, while Figure 36 gives and example of a training batch and a validation batch, respectively. Figure 36a demonstrates the mosaic data augmentation that was introduced in YOLOv8. Mosaic data augmentation is a technique where four different images are mixed together and provided to the model as input. This technique allows the model to learn the actual objects from different positions and with partial occlusion.

A.4.2 Results of data_all_640 model with unified labels

Figure 37 shows how the performance indicators evolve during the training process, while Figure 38 gives and example of a training batch and a validation batch, respectively. Figure 38a demonstrates the down-side of having many similar images that are taken from one video sequence – the validation set is very restricted and therefore not always representative to the wide range of possible scenarios.

A.4.3 Results of data_highres_railsem_640 model with separate labels

Figure 39 shows how the performance indicators evolve during the training process, while Figure 40 gives and example of a training batch and a validation batch, respectively. Figure **??** demonstrates the mosaic data augmentation that was introduced in YOLOv8. Mosaic data augmentation is a technique where four different images are mixed together and provided to the model as input. This technique allows the model to learn the actual objects from different positions and with partial occlusion.

A.4.4 Results of data_all_railsem_640 model with separate labels

Figure 41 shows how the performance indicators evolve during the training process, while Figure 42 gives and example of a training batch and a validation batch, respectively. Figure 46b demonstrates the down-side of having many similar images that are taken from one video sequence – the validation set is very restricted and therefore not always representative to the wide range of possible scenarios.

A.4.5 Parameter tuning with unified labels

Figure 43 and Figure 44 visualize the tuning process on the data_highres_railsem_640 model with AdamW and SGD optimizer, respectively. The parameters are described in Table 11. Certain parameters, such as degrees, translate, etc. are fixed at zero throughout the tuning process as it is unlikely that the resulting images appear in the real-world.

Figure 45 and Figure 46 visualize the tuning process on the data_highres_railsem_640 model with AdamW and SGD optimizer, respectively.

Train	Validation	Test
10_station_suelldorf_10.1	16_under_bridge_16.1	14_signals_station_14.1
11_main_station_11.1	18_vegetation_switch_18.1	21_station_wedel_21.1
12_vegetation_steady_12.1	1_calibration_1.2	4_station_pedestrian_bridge_4.2
13_station_ohlsdorf_13.1	3_fire_site_3.3	4_station_pedestrian_bridge_4.5
14_signals_station_14.2	9_station_ruebenkamp_9.1	7_approach_underground_station_7.2
14_signals_station_14.3	9_station_ruebenkamp_9.2	8_station_altona_8.3
15_construction_vehicle_15.1		
17_signal_bridge_17.1		
19_vegetation_curve_19.1		
1_calibration_1.1		
20_vegetation_squirrel_20.1		
21_station_wedel_21.2		
21_station_wedel_21.3		
2_station_berliner_tor_2.1		
3_fire_site_3.1		
3_fire_site_3.2		
3_fire_site_3.4		
4_station_pedestrian_bridge_4.1		
4_station_pedestrian_bridge_4.3		
4_station_pedestrian_bridge_4.4		
5_station_bergedorf_5.1		
5_station_bergedorf_5.2		
6_station_klein_flottbek_6.1		
6_station_klein_flottbek_6.2		
7_approach_underground_station_7.1		
7_approach_underground_station_7.3		
8_station_altona_8.1		
8_station_altona_8.2		
9_station_ruebenkamp_9.3		
9_station_ruebenkamp_9.4		
9_station_ruebenkamp_9.5		
9_station_ruebenkamp_9.6		
9_station_ruebenkamp_9.7		

Table 9: Dataset split: OSDaR23

Sensor	Mean	Median	Q1	Q5	Q95	Q10	Q90	Q99
ir_center	0.714	0.379	0.104	0.113	2.210	0.126	1.857	3.917
ir_left	1.215	1.082	0.121	0.344	2.315	0.451	2.293	2.591
ir_right	1.849	1.872	0.423	0.813	3.399	1.000	2.688	4.831
rgb_center	1.283	1.057	0.127	0.208	3.542	0.232	3.085	5.487
rgb_highres_center	0.671	0.618	0.066	0.071	1.804	0.073	1.561	2.620
rgb_highres_left	1.320	1.120	0.138	0.654	2.192	0.738	2.181	2.578
rgb_highres_right	1.623	1.191	0.169	0.607	3.627	0.690	3.580	4.324
rgb_left	2.151	1.815	0.353	0.700	3.882	0.873	3.845	5.632
rgb_right	2.522	1.890	0.143	0.951	5.515	1.329	4.101	8.476

Table 10: Bounding box aspect ratios for different sensors; Q* denotes quantile.

Parameter	Description
lr0	initial learning rate
lrf	final learning rate
momentum	SGD momentum/Adam beta1
weight_decay	optimizer weight decay
warmup_momentum	warmup initial momentum
box	box loss gain
cls	classification loss gain
dfl	dual focal loss gain
hsv_s	image Hue Saturation Value augmentation (fraction)
hsv_v	image Hue Saturation Value augmentation (fraction)
degrees	image rotation (+/- deg)
translate	image translation (+/- fraction)
shear	image shear (+/- deg)
perspective	image perspective (+/- fraction),
flipud	image flip up-down (probability)
fliplr	image flip left-right (probability)
mixup	image mixup (probability)
copy_paste	segment copy-paste (probability)

Table 11: Description of YOLO parameters

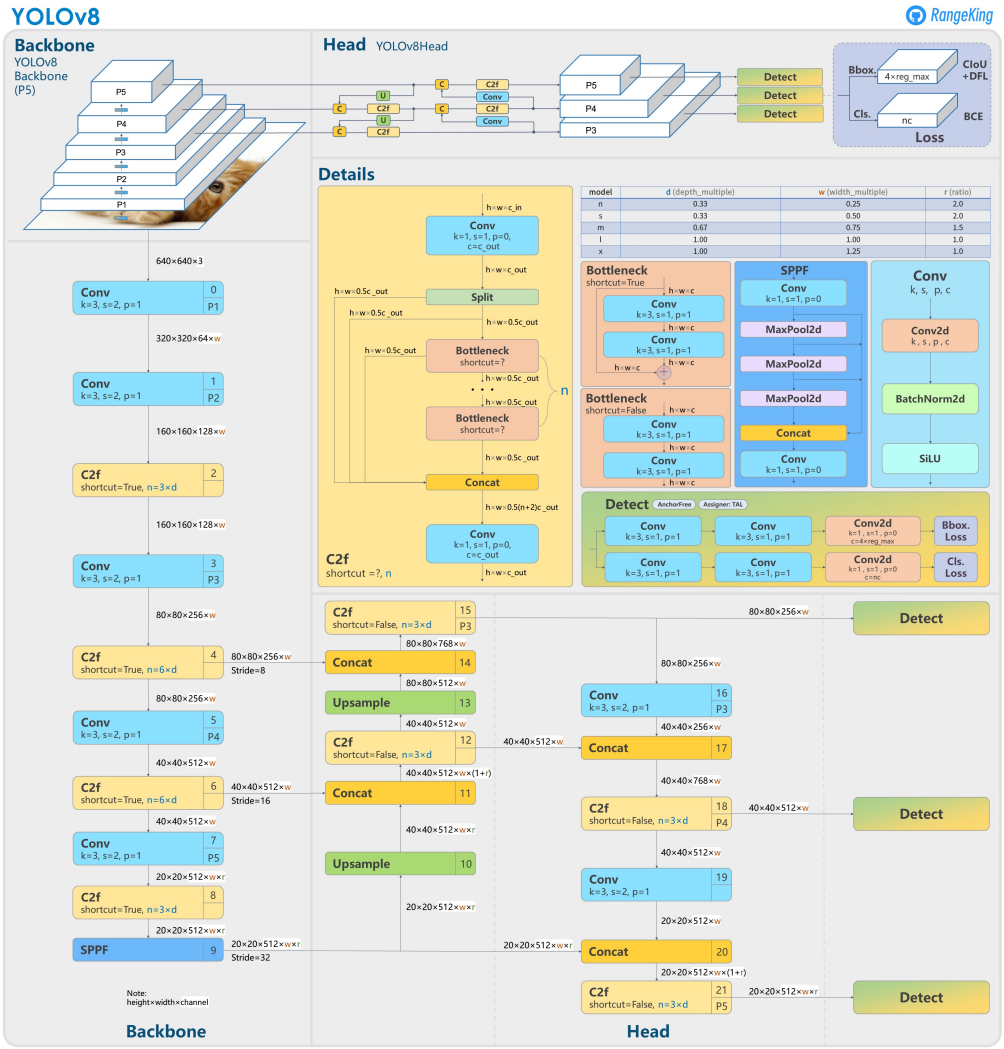

Figure 34: Model structure of YOLOv8 detection models.

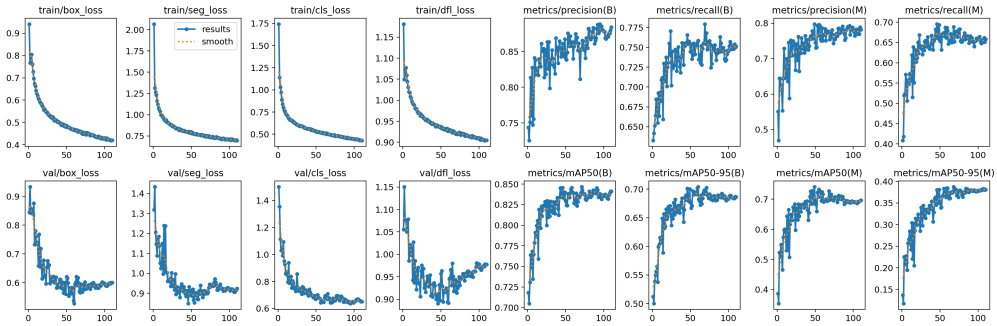

Figure 35: Training results of data_highres_railsem_640 model with unified labels. (B) stands for the results of the bounding box and (M) stands for the result of the segmentation mask.

(a) Example of training batch. Images are augmented.

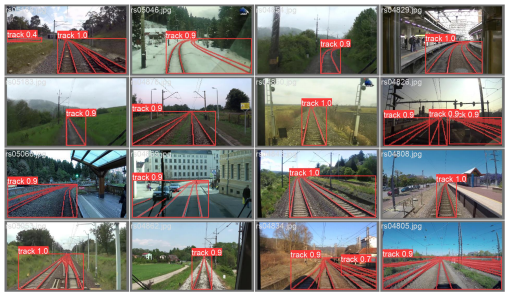

(b) Example of validation batch.

Figure 36: Example of training and validation batch during training model data_highres_railsem_640 with unified labels.

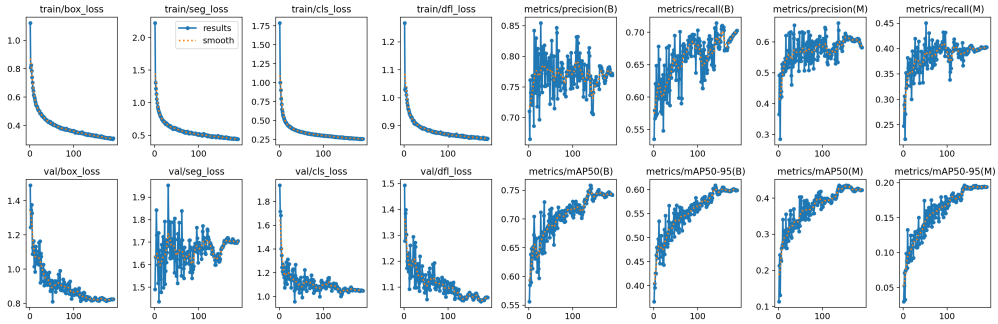

Figure 37: Training results of data_all_640 model with unified labels. (B) stands for the results of the bounding box and (M) stands for the result of the segmentation mask.

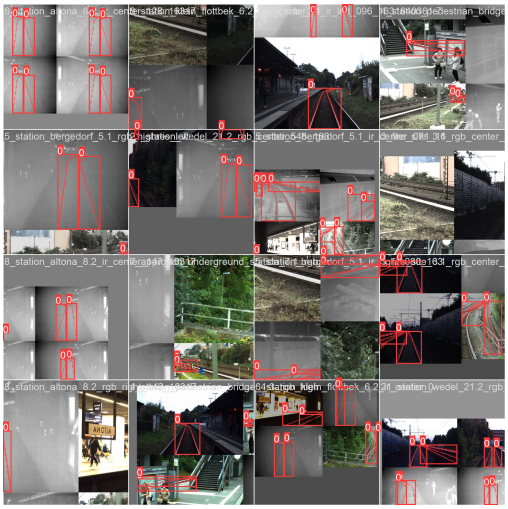

(a) Example of training batch. Images are augmented.

(b) Example of validation batch. Images are frames of video sequence.

Figure 38: Example of training and validation batch during training model data_all_640 with unified labels.

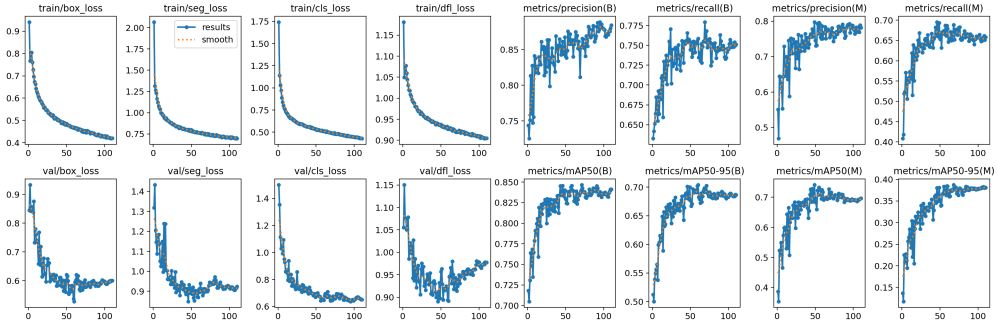

Figure 39: Training results of data_highres_railsem_640 model with separate labels. (B) stands for the results of the bounding box and (M) stands for the result of the segmentation mask.

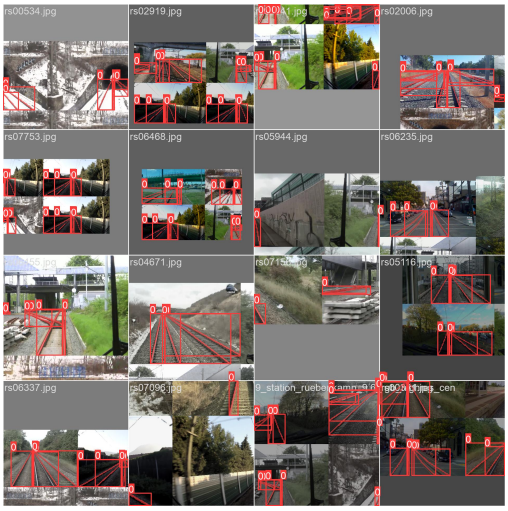

(a) Example of training batch. Images are augmented.

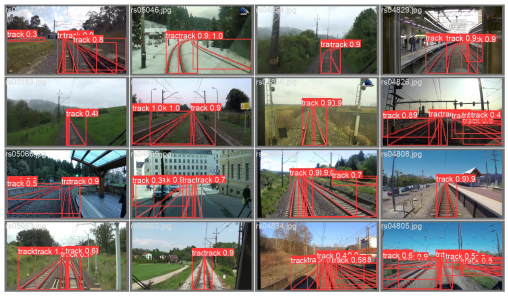

(b) Example of validation batch.

Figure 40: Example of training and validation batch during training model data_highres_railsem_640 with separate labels.

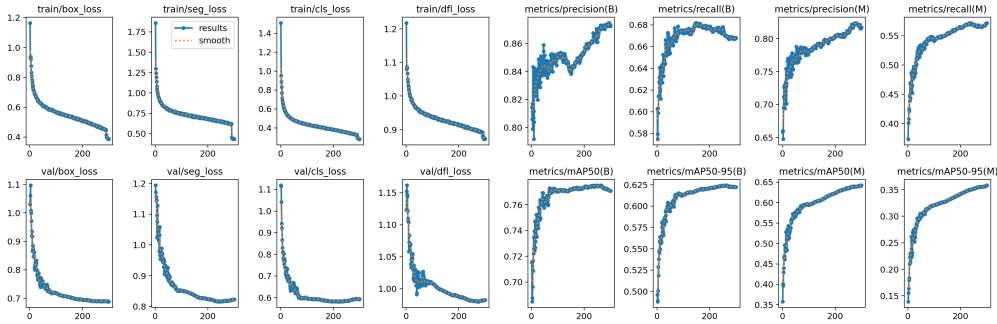

Figure 41: Training results of data_al_railsem_640 model with separate labels. (B) stands for the results of the bounding box and (M) stands for the result of the segmentation mask.

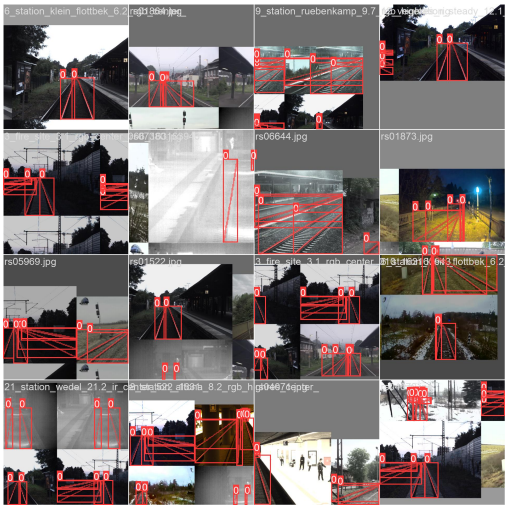

(a) Example of training batch. Images are augmented.

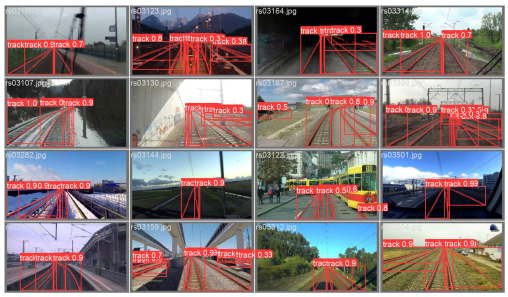

(b) Example of validation batch. Images are frames of video sequence.

Figure 42: Example of training and validation batch during training model data_all_railsem_640 with separate labels.

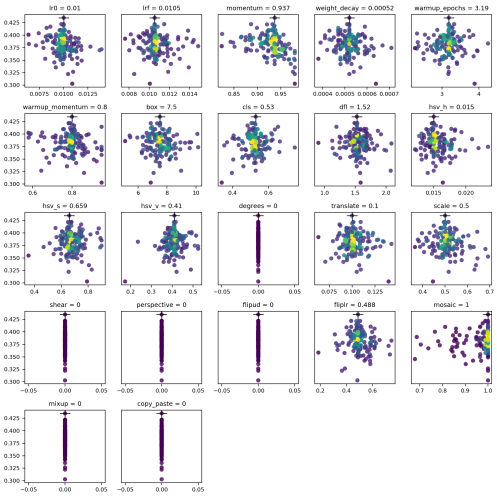

(a) Search space for different parameters. Density is distinguished by color: yellow shades indicate higher density

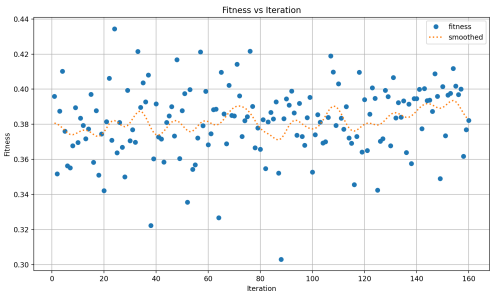

(b) Evolution of fitness value over 160 iterations. Model fitness is a weighted combination of different metrics (e.g., precision, recall, mAP@0.5).

Figure 43: Parameter tuning of model data_highres_railsem_640 with AdamW optimizer.

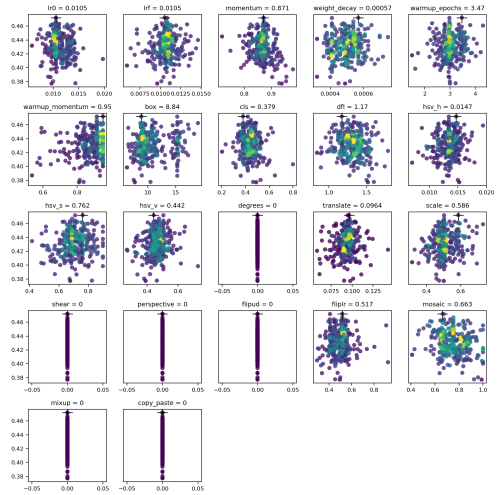

(a) Search space for different parameters. Density is distinguished by color: yellow shades indicate higher density

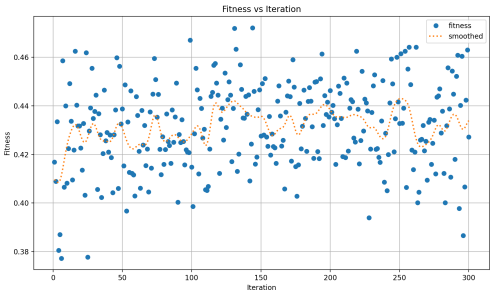

(b) Evolution of fitness value over 300 iterations. Model fitness is a weighted combination of different metrics (e.g., precision, recall, mAP@0.5).

Figure 44: Parameter tuning of model data_highres_railsem_640 with SGD optimizer.

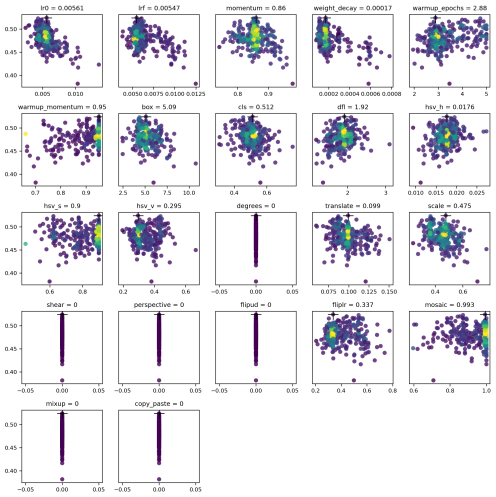

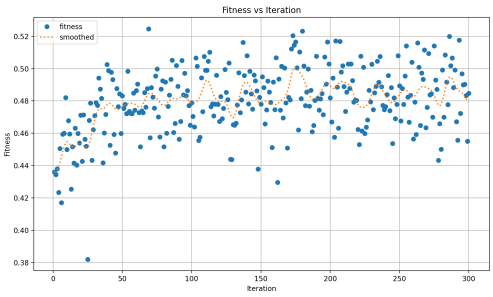

(a) Search space for different parameters. Density is distinguished by color: yellow shades indicate higher density

(b) Evolution of fitness value over 300 iterations. Model fitness is a weighted combination of different metrics (e.g., precision, recall, mAP@0.5).

Figure 45: Parameter tuning of model data_all_640 with AdamW optimizer.

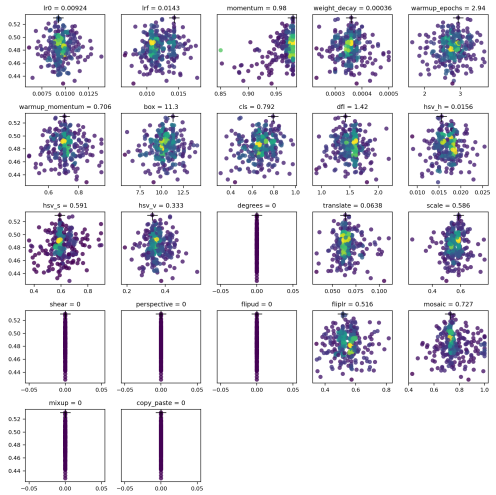

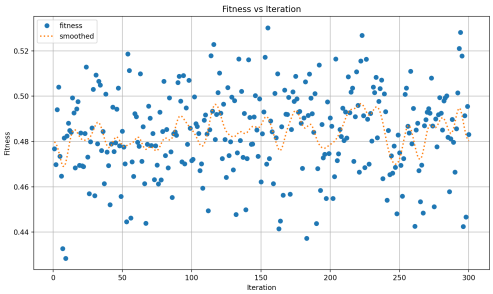

(a) Search space for different parameters. Density is distinguished by color: yellow shades indicate higher density

(b) Evolution of fitness value over 300 iterations. Model fitness is a weighted combination of different metrics (e.g., precision, recall, mAP@0.5).

Figure 46: Parameter tuning of model data_all_640 with SGD optimizer.